

Observable Signatures of RN Black Holes with Dark Matter Halos via Strong Gravitational Lensing and Constraints from EHT Observations

Niyaz Uddin Molla,^{1,*} Himanshu Chaudhary,^{2,†} Salvatore Capozziello,^{3,4,5,‡}
Farruh Atamurotov,^{6,§} G. Mustafa,^{7,8,¶} and Ujjal Debnath^{1,**}

¹Department of Mathematics, Indian Institute of Engineering Science and Technology, Shibpur, Howrah 711 103, India

²Department of Physics, Babeş-Bolyai University, Kogălniceanu Street, Cluj-Napoca, 400084, Romania,

³Dipartimento di Fisica “E. Pancini”, Università di Napoli “Federico II”,

Complesso Universitario di Monte Sant’ Angelo, Edificio G, Via Cinthia, I-80126, Napoli, Italy

⁴Scuola Superiore Meridionale, Largo S. Marcellino 10, I-80138, Napoli, Italy

⁵Istituto Nazionale di Fisica Nucleare (INFN), Sez. di Napoli,

Complesso Universitario di Monte Sant’ Angelo, Edificio G, Via Cinthia, I-80126, Napoli, Italy

⁶University of Tashkent for Applied Sciences, Str. Gavhar 1, Tashkent 100149, Uzbekistan

⁷Department of Physics, Zhejiang Normal University, Jinhua 321004, Peoples Republic of China

⁸Research Center of Astrophysics and Cosmology, Khazar University, Baku, AZ1096, 41 Mehseti Street, Azerbaijan

We explore the influence of dark matter halos on gravitational lensing produced by electrically charged, spherically symmetric black holes in the strong-field regime. This study delves into the strong gravitational lensing effects within the context of two significant dark matter models: the Universal Rotation Curve Model and the cold dark matter model. Initially, we derive the coefficients for the strong deflection limit and numerically analyze the substantial variations of the deflection angle. Additionally, we present graphical representations of these results. We find that the strong deflection angle, denoted as α_D , increases with the rising charge parameter magnitude Q in presence of a dark matter halo. Furthermore, we examine the various astrophysical consequences of the compact objects $M87^*$ and $SgrA^*$, as charged black holes, and compare results with those for other astrophysical black holes such as standard Reissner-Nordström (RN) and Schwarzschild black holes, via strong gravitational lensing observations. From our study, the observations point out that it may be possible to quantitatively differentiate and characterize charged black holes with dark matter halos from astrophysical black holes, such as the standard Reissner-Nordström and Schwarzschild black holes. Finally, We constrain the charge parameter Q with the observational data by the Event Horizon Telescope Collaboration for the supermassive black holes $M87^*$ and $SgrA^*$. We constrain the charge parameter Q of the charged black holes with universal rotation curve dark matter halo as $0 \leq |Q| \leq 0.366M$ for $M87^*$, $0 \leq |Q| \leq 0.586M$ for $SgrA^*$. The charged black hole with cold dark matter halo can be constrained with $0 \leq |Q| \leq 0.364M$ for $M87^*$, and $0 \leq |Q| \leq 0.584M$ for $SgrA^*$. It suggests that such charged black holes with dark matter halo satisfy the Event Horizon Telescope constraints. These results suggest, in principle, that it could be possible to identify charged black holes with dark matter halo in the future fine observational campaigns.

I. INTRODUCTION

The study of black hole (BH) spacetimes represents a crucial area of investigation within the realm of general relativity and other gravitational theories [1–4]. BHs offer a unique window into our understanding of gravitation, thermodynamics, and quantum effects in curved spacetime. Recent years have witnessed significant progress in both theoretical and observational

explorations of BHs. Notably, the LIGO and Virgo collaborations detected gravitational wave signals arising from the mergers of binary BHs [5–11]. Furthermore, there have been groundbreaking observations of high-resolution images of BHs at the center of our Milky Way galaxy, known as Sagittarius A* ($Sgr A^*$), which has indeed been a major focus of study and observation by the Event Horizon Telescope (EHT). The EHT captures high-resolution images of BHs. They also released the first-ever image of a BH, which is the supermassive BH in the center of the M87 galaxy [12].

BHs are classified into distinct types based on their properties, specifically mass, angular momentum (rotation), and electric charge. Firstly, Schwarzschild BHs [13], characterized by their mass and spherically

* niyazuddin182@gmail.com

† himanshu.chaudhary@ubbcluj.ro

‡ capozziello@na.infn.it (Corresponding author)

§ atamurotov@yahoo.com

¶ gmustafa3828@gmail.com (Corresponding author)

** ujjaldebnath@gmail.com

symmetric, non-rotating nature, represent the simplest and most fundamental type. These BHs are defined by the Schwarzschild solution and harbor an event horizon beyond which nothing, not even light, can escape. Second, Kerr BHs, known as rotating BHs, possess both mass and angular momentum, as described by the Kerr solution. They feature an event horizon and an ergosphere due to their rotation, introducing distinctive characteristics such as frame-dragging effects. Within the category of charged BHs, Reissner-Nordström (RN) BHs emerge as the third type. These BHs, encapsulated by the RN solution, carry both mass and electric charge, with this charge potentially being positive, negative, or zero.

Furthermore, dark matter (DM) is a fascinating and mysterious topic that continues to captivate researchers in various scientific fields, including astrophysics, cosmology, etc. There is a growing body of evidence supporting the existence of DM, which comes from sources like the unusual rotation patterns of spiral galaxies [14, 15], gravitational lensing effects [16], the formation of large-scale structures in the Universe [17], observations of the cosmic microwave background radiation [18, 19], and the study of baryon acoustic oscillations [20–22]. When we combine the data from studies on the cosmic microwave background, it becomes evident that approximately 26.8% of the Universe is composed by DM, while dark energy, generating the observed accelerated expansion of the cosmic flow, makes up a substantial 68.3% of the cosmic constituents [23]. The presence of DM has a significant and long-lasting impact on the evolution and ultimate destiny of our Universe, playing a crucial role in shaping the cosmos. The leading contenders for DM are theoretical particles proposed by theories that go beyond the Standard Model of particle physics. These potential candidates encompass weakly interacting massive particles (WIMPs) [24], axions [25], sterile neutrinos [26], dark photons [27], and millicharged particles [28]. However, beside several astrophysical and cosmological evidences, DM escapes, up to now, any probe at fundamental level so no final answer on its particle nature is today available. DM typically forms halo-like structures around galaxies [29, 30], intriguingly encompassing the supermassive BHs situated at their cores [31–34]. Hence, delving into and grasping the implications of DM halos on supermassive BHs in galactic centers holds paramount importance. In recent studies, researchers have delved into the influence of DM on the behavior of BHs. These investigations have spanned a wide range of subjects,

encompassing circular geodesics [35, 36], the formation of BH shadows [37–39], gravitational lensing [40], the dynamics of accretion disks [41–44], thermodynamics [4, 45], quasi-normal modes [46–48], the phenomenon of BH echoes [49], and even the complex processes of BH mergers. It is possible also to investigate alternative theories of gravity considering the BH shadows. See, e.g. Refs. [50–52]. Understanding the properties of DM, particularly its halo structures within galaxies, can be approached through various observational methods. Gravitational lensing is one of the most useful techniques in this regard. It is an extraordinary phenomenon rooted in Einstein’s theory of general relativity, which has immense implications for our understanding of the Universe [53, 54]. It occurs when massive objects, like galaxies or groups of galaxies, influence the very fabric of space and time, causing it to curve or bend. As a result, when light travels through this curved space, its path is altered, creating an effect akin to a cosmic magnifying glass. This lensing effect allows us to see and study distant celestial objects that would otherwise remain hidden from our view [55–57]. It aids us in the discovery of galaxies located far away from us, which would be nearly impossible to observe directly [58]. Moreover, it assists in mapping the distribution of DM, the enigmatic and elusive substance that makes up a substantial portion of the Universe mass [59, 60]. Gravitational lensing also plays a crucial role in the precise measurement of the Hubble constant [61]. It encompasses two main categories: weak lensing and strong lensing, each with its own distinct characteristics and applications. Weak lensing occurs when the gravitational influence of a massive object, like a galaxy or a galaxy cluster, subtly distorts the light from background objects. While the distortion is typically quite small, it provides invaluable insights into the distribution of matter in the foreground object and the larger cosmic structure. On the other hand, strong lensing involves more pronounced distortions in the path of light due to highly massive objects. This can create dramatic and often multiple images of a background object, such as a distant galaxy, around the massive foreground object. Strong lensing allows astronomers to probe the detailed properties of both the lensing object and the background sources. It has led to remarkable discoveries, such as the detection of distant galaxies and the study of the innermost regions of quasars. Over the past few decades, it has evolved into a crucial tool in astronomy and cosmology, enabling the test of gravity theories and astrophysical models [37, 62–74].

The concept of gravitational lensing was initially introduced within the weak field limit [75–78]. Subsequently, it garnered extensive exploration in the strong field limit [79–86]. Pioneering research by Darwin on the trajectories of photons in the vicinity of a BH revealed significant bending of light rays. The foundational work by [87] played a crucial role in establishing the groundwork for a precise lens equation. Subsequent numerical investigations, as discussed in [88, 89], focused on the lensing phenomenon induced by static, spherically symmetric naked singularities. These studies provided a comprehensive examination of various lensing observables. Building on these contributions, later in [90] explored gravitational lensing within spherically symmetric and static spacetime. Significantly, this exploration utilized the light-like geodesic equation without relying on approximations. The results derived from these investigations emphasize the profound importance of gravitational lensing, especially concerning BHs, underscoring its invaluable utility as a tool in astrophysics. Delving into the substantial gravitational effects near massive celestial bodies offers valuable insights into the characteristics of distant and faint stars. The phenomenon of gravitational lensing by various BHs has become a focal point in recent decades, underscoring its crucial role in astrophysical studies. Scientists have employed both functional and analytical approaches, drawing inspiration from the methods introduced in [85]. These approaches are based on the principle of the substantial bending of light rays. Through these methodologies, it has been discovered that as light rays approach the photon sphere of a Schwarzschild BH, the deflection angle undergoes a logarithmic divergence. This approach extends beyond Schwarzschild BHs and has been applied to various scenarios. For instance, it has been employed in the investigation of RN BHs [91] and implemented in metric systems characterized by staticity and spherical symmetry [92].

In depth exploration of gravitational lensing has emerged from the realization that analyzing the trajectories of light in the vicinity of BHs offers valuable perspectives on the intrinsic features of the surrounding spacetime. Researchers have delved into the phenomenon of gravitational lensing resulting from diverse sources, encompassing the distribution of cosmic structures [93–95], dark energy [96–98], DM [99–101], quasars [102–105], gravitational waves [106–108], and various other compact celestial objects [109–113]. A variety of investigations collectively enhance our comprehension of the complex interplay among matter, energy, and

spacetime. Notably, the Event Horizon Telescope collaboration has achieved a significant advancement in angular resolution. This breakthrough enables the observation of the supermassive BH situated at the core of the M87 galaxy. This remarkable achievement inaugurates a novel phase in exploring gravitational lensing within environments characterized by strong gravitational fields. [114–118]. Moreover, the utilization of relativistic images for investigating gravity under strong deflection conditions has found application in diverse BH metrics. This encompasses examinations in both the framework of general relativity and modified gravitational theories. Numerous scholars have made significant contributions to this realm, as evident in [119–125]. In this study, our aim is to thoroughly examine two models of DM halos within the framework of strong gravitational lensing, specifically in the context of static and charged spacetime.

The structure of this paper is organized as follows: Section II provides a brief overview of the structure of the RN BH spacetime in the presence of DM halos. Moving on to Section III, we delve into the gravitational lensing phenomena induced by BHs, detailing aspects such as the lens equation, deflection angle, and strong lensing coefficients. This section focuses in particular on two supermassive BHs $M87^*$ and $SgrA^*$ within the framework of charged BHs accompanied by DM halos. We explore various strong lensing observables, including the angular position of the innermost image, image separation for the first and n^{th} relativistic images, brightness differences among these images, and the time delay between the first and second relativistic images. Section IV conducts a comparative analysis of strong lensing observables, contrasting the outcomes between standard Schwarzschild BH, standard RN BH, and charged BH spacetime coupled with a DM halo. In this comparative study two distinct models, the universal rotation curve (URC) and cold dark matter (CDM) halo with the Navarro-Frenk-White (NFW) profile are considered. Moving forward, Section V is dedicated to constraining the charge parameter Q with DM halos based on observational data from the Event Horizon Telescope (EHT) for both $M87^*$ and $SgrA^*$. Finally, in Section VI, we encapsulate our key findings and draw conclusions from the study.

II. BLACK HOLE GEOMETRY AND DARK MATTER HALO

To examine the geometry around the BH in this section, we initiate our analysis with a spherically symmetric static spacetime characterized by the following metric:

$$ds^2 = -f(r)dt^2 + \frac{1}{f(r)}dr^2 + r^2d\theta^2 + r^2\sin^2\theta d\varphi^2, \quad (1)$$

The BH lapse function is defined as $f(r)$ in the above equation. This study will center around the examination of the lapse function described in: [44, 126]:

$$f(r) = 1 - \frac{2MG_N}{c^2r} + \frac{Q^2}{r^2}, \quad (2)$$

where $Q^2 = (q^2G_N)/(4\pi\epsilon_0c^4)$. In addition, q and M represent the charge and mass of BH. Now, we shall incorporate the URC profile and CDM halo with NFW profile into the above BH geometry to see how they affect the BHs solutions. It is worth noticing that charged BH solutions constitute, today, a very active research area due to their interesting properties in standard GR and in alternative gravities [127–130].

A. Universal Rotation Curve Profile

The well-known DM halo-like URC profile will be briefly discussed here in this subsection. According to [131], the following equation characterizes the distribu-

$$f(r) = \left(1 - 2\pi^2AB\right) \left(1 - 4\pi AB \left(\frac{Br}{M} + 1\right)\right) \left(4\pi AB \left(\frac{Br}{M} + 1\right) + 1\right) \left(\frac{2\pi AB^2r(Br - M)}{M^2} + 1\right) - \frac{2M}{r} + \frac{Q^2}{r^2}. \quad (5)$$

In the above Eq. (5), we have two new parameters namely A and B . For the current analysis, both are calculated as $A = \frac{\rho_0 r_0^3}{M}$ and $B = \frac{MG_N}{c^2 r_0}$. Parameters A and B are determined now using the observationally well-fit values for M87*, as follows: $B = \frac{MG_N}{c^2 r_0} = 3.40611 * 10^{-9}$ and $A = \frac{\rho_0 r_0^3}{M} = 805.231$. For Sgr A*, A and B are measured as: $B = \frac{MG_N}{c^2 r_0} = 2.6346 * 10^{-11}$, $A = \frac{\rho_0 r_0^3}{M} = 5738.77$.

tion of URC profile

$$\rho(r) = \frac{\rho_0 r_0^3}{(r + r_0)(r^2 + r_0^2)}, \quad (3)$$

where ρ_0 and r_0 express the central density and the characteristic radius of the URC DM halo. The best fit values for ρ_0 and r_0 was given in [132, 133] by using the the recent observations. For the M87* galaxy in the framework of URC DM profile, the involved parameters are measured as: $\rho_0 = 6.9 * 10^6 M_\odot / \text{kpc}^3$ and $r_0 = 91.2$ kpc. For the other case, i.e., Milky Way galaxy $\rho_0 = 5.2 * 10^7 M_\odot / \text{kpc}^3$ and $r_0 = 7.8$ kpc [134] are measured. Within the scenario of URC DM profile, the lapse function $f(r)$ [135] from the metric Eq (2) is revised as:

$$f(r) = e^{-\frac{2\pi^2\rho_0 r_0^2 G_N}{c^2} \left(\frac{r^2}{r_0^2} + 1\right) - \frac{(1-\frac{r}{r_0})(2\pi\rho_0 r_0^3 G_N)}{c^2 r}} \times \left(\frac{r}{r_0} + 1\right)^{-\frac{(r/r_0+1)(4\pi\rho_0 r_0^3 G_N)}{c^2 r}} \times e^{\frac{4\pi\rho_0 r_0^3 G_N \tan^{-1}\left(\frac{r(r/r_0+1)}{r_0}\right)}{c^2 r} - \frac{2MG_N}{c^2 r} + \frac{Q^2}{r^2}}. \quad (4)$$

In the above relation, we shall consider $M = 4.3 * 10^6 M_\odot$ for the Sgr A* BH and $M = 6.5 * 10^9 M_\odot$ for the M87* central BH according to [135]. In Eq. (4), the lapse function is very complicated. For the present study, we shall discuss strong gravitational lensing by using the series solution alone for the sake of simplicity, which may be computed directly as:

B. The Cold Dark Matter Halo with Navarro Frenk White Profile

The CDM halo model with NFW profile was constructed by using N -body simulations, commonly known as the universal spherically averaged density profile [136], and is stated as:

$$\rho(r) = \frac{\rho_0}{(r/r_0)(1+r/r_0)^2}, \quad (6)$$

where ρ_0 and r_0 define the density of the universe of halo and characteristic radius respectively at the stage

of collapsing. As per the latest observational findings related to the Milky Way galaxy [134], the optimal numerical values for the parameters ρ_0 and r_0 are determined when considering the influence of CDM halo characterized by the NFW profile are measured as $\rho_0 = 5.23 \times 10^7 M_\odot/\text{kpc}^3$ and $r_0 = 8.1$ kpc. For the M87* BH model, these values are measured as $\rho_0 = 0.008 \times 10^{7.5} M_\odot/\text{kpc}^3$ (see [137] and $r_0 = 130$ kpc [135]. Within the context of the CDM halo profile, [138] provides the following expression for the function $f(r)$ in the metric defined by Eq. (2) as

$$f(r) = \left(1 + \frac{r}{r_0}\right)^{-\frac{8\pi G_N \rho_0 r_0^3}{c^2 r}} - \frac{2G_N M}{c^2 r} + \frac{Q^2}{r^2}, \quad (7)$$

The central BH mass for M87*, denoted as M , is $6.5 \times 10^9 M_\odot$, and for the Sgr A* BH model, the specific mass is $M = 4.3 \times 10^6 M_\odot$. When considering strong gravitational lensing, the expression in Eq. (7) becomes notably intricate due to the exponential function in the lapse function as defined by Eq. (2). To address this complexity, it is essential to employ a series solution for the present BH lapse function, taking into account the influence of the CDM halo model with a NFW profile. The updated form of the lapse function is now given by

$$f(r) = 1 - \frac{2M}{r} + 32\pi^2 A^2 B^2 + \frac{4\pi AB(Br + 2M)}{M} + \frac{Q^2}{r^2}. \quad (8)$$

$$P(r) = \left(1 - 2\pi^2 AB\right) \left(4\pi AB^2 r(2Br - 1) + 1\right) \left(4\pi AB(2Br + 1) + 1\right) \left(1 - 4\pi AB(2Br + 1)\right) + \frac{Q^2}{r^2} - \frac{1}{r}. \quad (10)$$

For the above relation values of the parameters A and B for M87* are measured as: $A = \frac{\rho_0 r_0^3}{M} = 85.508$; $B = \frac{MG_N}{c^2 r_0} = 2.38952 * 10^{-9}$. For the Sgr A* BH model values of A and B are calculated as: $A = \frac{\rho_0 r_0^3}{M} = 6463.81$; $B = \frac{MG_N}{c^2 r_0} = 2.537 * 10^{-11}$.

III. STRONG GRAVITATIONAL LENSING EFFECTS BY CHARGED BLACK HOLES WITH DARK MATTER HALOS

Here, we shall study strong gravitational lensing by BHs using two different DM halo models. The first case involves charged BHs with the URC DM halo model, and the second case concerns charged BHs with the CDM halo model. To do this, we investigate the deflection of photon rays by charged BHs with the URC and CDM DM halo models in the equatorial plane ($\theta = \frac{\pi}{2}$), ensuring that both the observer and source lie in the same plane. To study the strong deflection angle of photon rays, we first rewrite Eq (1) through the following transformations $t \rightarrow \frac{t}{2M}$, $r \rightarrow \frac{r}{2M}$, $Q \rightarrow \frac{Q}{2M}$ as:

$$d\bar{s}^2 = -P(r)dt^2 + R(r)dr^2 + S(r)d\phi^2. \quad (9)$$

With the help of Eq (5), one can express the metric coefficient functions for a charged BH with the URC DM halo within the framework of Eq (9) as follows:

and

$$R(r) = \left[\left(1 - 2\pi^2 AB\right) \left(4\pi AB^2 r(2Br - 1) + 1\right) \left(4\pi AB(2Br + 1) + 1\right) \left(1 - 4\pi AB(2Br + 1)\right) + \frac{Q^2}{r^2} - \frac{1}{r} \right]^{-1}. \quad (11)$$

$$S(r) = r^2. \quad (12)$$

and using Eq (8), the metric coefficient functions for a charged BH with the CDM DM halo with NFW profile model within the framework of Eq (9) as :

$$P(r) = 1 - \frac{1}{r} + \frac{Q^2}{r^2} + 32\pi^2 A^2 B^2 + 8\pi AB(Br + 1), \quad (13)$$

$$R(r) = \left[1 - \frac{1}{r} + \frac{Q^2}{r^2} + 32\pi^2 A^2 B^2 + 8\pi AB(Br + 1) \right]^{-1}, \quad (14)$$

$$S(r) = r^2. \quad (15)$$

By employing the Eq denoted as Eq. (9), it is possible to deduce null geodesics in relation to the affine parameter τ through the following set of Eqs.

$$\dot{t} = \frac{dt}{d\tau} = \frac{E}{P(r)} \quad (16)$$

$$\dot{\phi} = \frac{d\phi}{d\tau} = \frac{L}{r^2} \quad (17)$$

$$\left(\frac{dr}{d\tau}\right)^2 = \dot{r}^2 = E^2 - \frac{L^2}{r^2}P(r) \quad (18)$$

In the given context, E represents the total energy of the test particle, while L denotes the angular momentum of the particle. These parameters are associated with the ∂_t and ∂_ϕ killing vectors, respectively. The function $P(r)$, a metric component, is given by the Eqs (10) and (13) for the URC and CDM halo models, respectively. Eq (18) can be expressed as

$$\left(\frac{dr}{d\tau}\right)^2 + V_{eff} = E^2 \quad (19)$$

where the effective potential of a photon is expressed by the following expression

$$V_{eff} = \frac{L^2}{r^2}P(r) \quad (20)$$

To determine the radius r_{ph} of the unstable circular photon orbit, certain conditions on the effective potentials must be satisfied. Specifically, the conditions are that the first derivative of the effective potential with respect to r , evaluated at r_{ph} , must be equal to zero ($\left.\frac{dV_{eff}}{dr}\right|_{r_{ph}} = 0$), and the second derivative of the effective potential with respect to r , also evaluated at r_{ph} , must be less than zero ($\left.\frac{d^2V_{eff}}{dr^2}\right|_{r_{ph}} < 0$). Therefore, the photon sphere radius r_{ph} is identified as the real root of the following expression [80, 139, 140]:

$$2P(r_{ph}) - r_{ph}P'(r_{ph}) = 0 \quad (21)$$

It is noteworthy that at the photon sphere radius, denoted as r_{ph} , the condition $\left.\frac{d^2V_{eff}}{dr^2}\right|_{r_{ph}} < 0$ is satisfied in the context of the charged BH spacetime incorporating URC and CDM models, as described in Eq (9). The fulfillment of this condition implies the instability of these orbits against small perturbations. In this scenario, photons originate from infinity, nearing the BH with a certain impact parameter u and subsequently recede to infinity after reaching their closest approach, denoted as

r_0 . At this minimum distance, where $\frac{dr}{d\tau} = 0$, we can express the ratio $\frac{L}{E}$ as a function of the impact parameter “ u ” in relation to the closest distance r_0 as [92]

$$u = \frac{L}{E} = \frac{r_0}{\sqrt{P(r_0)}} \quad (22)$$

The strong deflection angle grows unboundedly as r_0 approaches r_{ph} , and it remains finite only when $r_0 > r_{ph}$. Therefore, the critical impact parameter, denoted as u_{ph} , is described by

$$u_{ph} = \frac{r_{ph}}{\sqrt{P(r_{ph})}} \quad (23)$$

For impact parameters u less than u_{ph} , photons experience gravitational attraction towards the BH. Conversely, when the impact parameter exceeds u_{ph} , photons approach their minimum distance to the BH, denoted as r_0 . At the critical point where the impact parameter u equals u_{ph} , photons initiate an unstable circular orbit around the BH, creating a photon sphere characterized by a radius of r_{ph} . By solving the null geodesic equations, the expression for the strong deflection angle of a photon originating from infinity, within the framework of charged BH spacetime, as described by Eq. (9), can be formulated as follows [88].

$$\alpha_D(r_0) = I(r_0) - \pi \quad (24)$$

where

$$I(r_0) = 2 \int_{r_0}^{\infty} \frac{d\phi}{dr} dr \quad (25)$$

or,

$$I(r_0) = \int_{r_0}^{\infty} \frac{2\sqrt{R(r)}dr}{\sqrt{S(r)}\sqrt{\frac{P(r_0)S(r)}{S(r)S(r_0)} - 1}} dr \quad (26)$$

In the given context, r_0 represents the closest approach distance of the photon’s trajectory. It is important to highlight that the magnitude of the strong deflection angle, denoted as $\alpha_D(r_0)$, is influenced by the interplay between r_{ph} and r_0 . When r_0 approaches the vicinity of r_{ph} , a notable enhancement in the deflection angle is observed. To address this relationship more explicitly, we introduce a novel parameter, designated as “ z ,” drawing inspiration from previous scholarly works [141, 142]

$$z = 1 - \frac{r_0}{r} \quad (27)$$

and obtain

$$I(r_0) = \int_0^1 F(z, r_0)H(z, r_0)dz \quad (28)$$

where

$$F(z, r_0) = \frac{2(1 - P(r_0))\sqrt{S(r_0)}}{S(r)A'(r)}\sqrt{P(r)R(r)}, \quad (29)$$

$$H(z, r_0) = \frac{\sqrt{S(r)}}{\sqrt{S(r)P(r_0) - P(r)S(r_0)}} \quad (30)$$

The function $F(z, r_0)$ exhibits regular behavior for all values of z and r_0 , in contrast to the function $H(z, r_0)$, which diverges as z approaches zero. The integral given by Eq (28) can be appropriately defined in this context.

$$I(r_0) = I^D(r_0) + I^R(r_0) \quad (31)$$

where the regular part and the divergent part of the integral are

$$I^R(r_0) = \int_0^1 g(z, r_0) dz \quad (32)$$

$$I^D(r_0) = \int_0^1 F(0, r_{ph})H_0(z, r_0) dz \quad (33)$$

and $g(z, r_0) = F(z, r_0)H(z, r_0) - F(0, r_{ph})H_0(z, r_0)$. To determine the order of divergence of the integrand in Eq (33), one can express the term inside the square root of $H_0(z, r_0)$ as follows:

$$H_0(z, r_0) = \frac{1}{\sqrt{\eta(r_0)z + \zeta(r_0)z^2 + \mathcal{O}(z^3)}} \quad (34)$$

where

$$\eta(r_0) = \frac{(1 - P(r_0))}{P'(r_0)S(r_0)} \left(P(r_0)S'(r_0) - P'(r_0)S(r_0) \right) \quad (35)$$

$$\zeta(r_0) = \frac{(1 - P(r_0))^2}{P'^3(r_0)S^2(r_0)} \left(2S(r_0)S'(r_0)P'(r_0)^2 + (S(r_0)S''(r_0) - 2S'^2(r_0))P(r_0)P'(r_0) - S(r_0)S'(r_0)P(r_0)P''(r_0) \right) \quad (36)$$

In the given context, the prime symbol signifies differentiation concerning the variable r . When r_0 is approximately equal to r_{ph} , the coefficient $\eta(r_0)$ becomes zero, resulting in a divergence order of z^{-1} . This divergence leads to a logarithmic divergence of the integral. When

r_0 is close to r_{ph} , the expression for the deflection angle can be articulated as follows [141–145]

$$\alpha(u) = -\bar{a} \log \left(\frac{u}{u_{ph}} - 1 \right) + \bar{b} + \mathcal{O}((u - u_{ph}) \log(u - u_{ph})) \quad (37)$$

where

$$\bar{a} = \frac{F(0, r_{ph})}{2\sqrt{\zeta(r_{ph})}} = \sqrt{\frac{2P(r_{ph})R(r_{ph})}{P(r_{ph})S''(r_{ph}) - P''(r_{ph})S(r_{ph})}} \quad (38)$$

and

$$\bar{b} = -\pi + a_R + \bar{a} \log \left(\frac{4\zeta(r_{ph})S(r_{ph})}{u_{ph}|P(r_{ph})|(2u_{ph}P(r_{ph}))} \right), \quad (39)$$

$a_R = I^R(r_{ph}) = \int_0^1 g(z, r_{ph}) dz$ which is numerically obtained. Now, we explore the diverse astrophysical implications through the observation of strong gravitational lensing. In this investigation, we focus on a scenario characterized by a high alignment of the source, the lens (BH), and the observer. Additionally, both the observer and the source are positioned at considerable distances from the BH. Consequently, the lens equation governing strong gravitational lensing can be formulated as follows [85]

$$\beta = \tilde{\alpha} - \frac{D_{ls}}{D_{os}} \Delta\alpha_n \quad (40)$$

The symbols D_{ls} and D_{os} denote the lens-source, and observer-source distance, respectively, where $D_{os} = D_{ol} + D_{ls}$. The parameter β represents the angular separation between the lens (BH), while $\tilde{\alpha}$ represents the angular separation between the source of the image and the lens relative to the optical axis. The offset of the deflection angle is given by $\Delta\alpha_n = \tilde{\alpha} - 2n\pi$, where n is an integer. Utilizing Eqs (37) and (40), the angular position of the n^{th} relativistic image can be approximated as follows:

$$\theta_n = \theta_n^0 - \frac{u_{ph}e_n D_{os}(\theta_n^0 - \beta)}{\bar{a}D_{ls}D_{ol}} \quad (41)$$

where

$$e_n = e^{\frac{\bar{b} - 2n\pi}{\bar{a}}},$$

$$\theta_n^0 = \frac{u_{ph}(1 + e_n)}{D_{ol}},$$

θ_n^0 is the image position corresponding to $\alpha = 2n\pi$. The magnification of n -th relativistic image, is expressed as [92]

$$\mu_n = \left(\frac{\beta}{\tilde{\alpha}} \frac{d\beta}{d\tilde{\alpha}} \right)^{-1} \Big|_{\theta_n^0} = \frac{e_n u_{ph}^2 (1 + e_n) D_{os}}{\bar{a} \beta D_{ls} D_{ol}^2} \quad (42)$$

It is important to highlight that the initial relativistic image exhibits the highest brightness, and its magnification undergoes an exponential decline as n increases. Particularly, when $\beta \rightarrow 0$, Eq (42) exhibits divergence. Therefore, achieving precise alignment significantly improves the probability of detecting relativistic images. If we denote θ_n as the asymptotic position where a cluster of images converges as n approaches infinity, then the brightest image, specifically the outermost image labeled as θ_1 , can be uniquely identified. Simultaneously, all inner images converge closely together at the position θ_∞ . Utilizing the strong deflection angle, as elaborated in Eq (37), and the lens equation for strong gravitational lensing given in Eq (40), we have derived three observable quantities: the angular position of the set of asymptotic relativistic images, denoted as θ_∞ ; the angular separation S between the outermost image (θ_1) and the closely packed inner images (θ_∞); and the relative magnification of the outermost relativistic image compared to the remaining relativistic images. [92, 146]

$$\theta_\infty = \frac{u_{ph}}{D_{ol}} \quad (43)$$

$$S = \theta_1 - \theta_\infty \approx \theta_\infty e^{\frac{(\tilde{b}-2\pi)}{\tilde{a}}} \quad (44)$$

$$r_{mag} = \frac{\mu_1}{\sum_{n=2}^{\infty} \mu_n} \approx \frac{5\pi}{\tilde{a} \log(10)} \quad (45)$$

Upon assessing the measurable parameters θ_∞ , S , and r_{mag} , the lensing coefficients \tilde{a} , \tilde{b} , and u_{ph} can be deduced utilizing Eqs (43), (44), and (45). The obtained values can then be juxtaposed with the predictions from theoretical models. This comparison allows for the characterization of charged BHs with DM halos surrounding other astrophysical BHs. In scenarios where the source, BH (lens), and observer are in alignment, denoted by $\beta = 0$ in Eq. (41), the BH (lens) alters the trajectory of light rays in all directions, resulting in the formation of a ring-shaped image known as an Einstein ring. [93, 94, 147–150]. By simplifying the Eq (25) for the case where $\beta = 0$, the resulting formula provides the angular radius of the n^{th} relativistic image.

$$\theta_n = \theta_n^0 \left(1 - \frac{u_{ph} e_n D_{os}}{\tilde{a} D_{ls} D_{ol}} \right) \quad (46)$$

In the scenario where the BH (acting as a lens) is positioned at a midpoint between the source and receiver, denoted as $D_{os} = 2D_{ol}$, and assuming that D_{ol} significantly exceeds the photon impact parameter u_{ph} , the angular radius of the n^{th} relativistic Einstein ring within

the framework of a modified Bardeen BH can be expressed as follows:

$$\theta_n^E = \frac{u_{ph}(1 + e_n)}{D_{ol}} \quad (47)$$

Time delay, denoted as $\Delta T_{2,1}$, emerges as a crucial and significant observable in the context of strong lensing. It characterizes the time lag between the formation of two relativistic images, accounting for fluctuations in the source's luminosity. The varying travel times for photons along their distinct paths create temporal disparities among different relativistic images. This temporal offset becomes a pivotal parameter, rooted in the fluctuations in the times of image formation. The ability to differentiate between the temporal signals of primary and secondary images during observational studies allows for the computation of the time delay between these signals [120]. While a photon makes its journey from the source to an observer, the duration it requires to complete an orbit around the BH can be calculated using the formula proposed by [120].

$$\tilde{T} = \tilde{a} \log \left(\frac{u}{u_{ph}} - 1 \right) + \tilde{b} + \mathcal{O}(u - u_{ph}) \quad (48)$$

By employing the Eq (48), one can calculate the time delay between two relativistic images. In the context of a spherically symmetric spacetime, the time delay between two images, when both images occur on the same side of the BH, can be formulated as per [120].

$$\Delta T_{2,1} = 2\pi u_{ph} = 2\pi D_{ol} \theta_\infty \quad (49)$$

By utilizing Eq (49), if we make precise estimations of the time delay and critical impact parameter, it becomes possible to derive the distance of the BH with negligible error. This study focuses on the assessment of the time delay between images produced through strong field lensing caused by a charged BH, considering the influence of the URC and CDM DM halo. The investigation is specifically conducted in the context of two supermassive BHs, denoted as $M87^*$ and $SgrA^*$.

A. URC profile

In this subsection, we investigate the strong gravitational lensing by charged BHs with a URC DM halo and its various astrophysical consequences in the context of two supermassive BHs $M87^*$ and $SgrA^*$. Furthermore, we compare the strong gravitational lensing phenomena by charged BH with a URC DM halo with the standard RN, as well as standard Schwarzschild BHs. The radius

of the photon sphere r_{ph}/R_s in Fig. 1(a) and the impact parameter u_{ph}/R_s in Fig. 1(b) are depicted as functions of the charge parameters Q for the URC model. From Figs. 1(a) & 1(b), it is found that the radius of the photon sphere r_{ph} and the impact parameter u_{ph}/R_s decrease with charge parameters Q . Furthermore, the impact parameter u_{ph}/R_s for the case of a charged BH with a URC DM halo is slightly greater than the case of the standard RN ($Q = 0.3$) and smaller than the case of standard Schwarzschild BHs see Fig. 1(b) and Table I & II. The deflection limit coefficients \bar{a} and \bar{b} for the case of the URC DM model as functions of the charge parameter Q are respectively displayed in Figs. 2(a) and 2(b). It is observed that the deflection limit coefficient \bar{a} increases with Q , while the deflection limit coefficient \bar{b} first increases with Q , then reaches its maximum value, and then decreases with Q . The strong deflection angle α_D for the case of the URC DM model as a function of the charge parameter Q is displayed in Fig. 3(a), and as a function of the impact parameter u with different values of the charge parameter Q is displayed in Fig. 3(b). In Fig. 3(a), it is seen that the deflection angle α_D increases with the magnitude of the charge parameter Q . The deflection angle α_D for the case of a charged BH with a URC DM halo (black solid line) is slightly greater than the case of the standard RN (green solid line) as well as standard Schwarzschild (red solid line) BHs. Moreover, the strong deflection angle α_D for the URC DM model decreases with the minimum impact parameter u , and the strong deflection angle α_D diverges at the critical impact parameter $u = u_{ph}$ at the photon radius $r = r_{ph}$ see Fig.3(b). From Table III and Figs. 4 & 5, it is found that the angular image position θ_∞ and relative magnification r_{mag} decrease with the parameter Q . In contrast, the observable quantity, the angular image separation S for the case of a charged BH with a URC DM halo is slightly greater than the cases of standard RN as well as for the cases of Schwarzschild BH with a halo and standard Schwarzschild BHs see Fig. 5(a) & 5(b) and Table III. Still, the angular separation S increases with the parameter Q . Furthermore, the observable quantity, the angular image position θ_∞ for the case of a charged BH with a URC DM halo is slightly greater than that for the standard RN BH ($Q = 0.3$) and smaller than those for the cases of Schwarzschild BH with a halo, as well as standard Schwarzschild BHs see Fig. 4(a) & 4(b) and Table III. Meanwhile, the observable quantity, the angular image separation S for the case of a charged BH with a URC DM halo is slightly greater than the cases of standard RN, as well as for the cases of Schwarzschild BH with a halo and standard Schwarzschild BHs see Fig. 5(a) & 5(b) and Table III. However, the observ-

able quantity, the relative magnification r_{mag} for the case of a charged BH with a URC DM halo is slightly smaller than the cases of standard RN, as well as for the cases of Schwarzschild BH with a halo and standard Schwarzschild BHs see Fig. 6 and Table III. It is important to emphasize that the photon sphere radius r_{ph}/R_s , the minimum impact parameter u_{ph}/R_s , strong deflection limit coefficients \bar{a} and \bar{b} , strong deflection angle α_D , and the lensing observable quantity, the relative magnification r_{mag} for the case of a charged BH with a URC DM halo exhibit nearly identical characteristics for the $M87^*$ and $SgrA^*$ scenarios. In Figs. 7(a) & 7(b), the outermost relativistic Einstein rings (θ_n^E) of $M87^*$ and $SgrA^*$ have been depicted for the case of a charged BH with a URC DM halo, standard RN, Schwarzschild BH with a halo, and standard Schwarzschild BH. It has been observed that the Einstein ring radius is slightly smaller in the cases of the standard RN BH (with $Q=0.2$) and in the cases of Schwarzschild BHs with a halo compared to standard Schwarzschild BHs. In Figs. 8(a) & 8(b), We plot the time delays $\Delta T_{2,1}$ between two different relativistic images. From these figures and Table. III, it is evident that the time delays $\Delta T_{2,1}$ between two different relativistic images decrease with the parameter Q in the context of the $M87^*$ and $SgrA^*$ BHs with a URC DM halo. Furthermore, it is observed that the time delays $\Delta T_{2,1}$ are smaller than those in the cases of the standard RN BH ($Q=0.2$), as well as in the cases of Schwarzschild BHs with a halo and standard Schwarzschild BH.

B. CDM halo with NFW profile

In this subsection, we investigate strong gravitational lensing by a charged BH with a CDM halo and explore its various astrophysical consequences in the context of two supermassive BHs, $M87^*$ and $SgrA^*$. Additionally, we compare the strong gravitational lensing phenomena by a charged BH with a CDM halo with standard RN, as well as standard Schwarzschild BHs. The radius of the photon sphere r_{ph}/R_s in Fig. 9(a) and the impact parameter u_{ph}/R_s in Fig. 9(b) are depicted as functions of charge parameters Q for the URC model. From Figs. 9(a) & 9(b), we observe that the radius of the photon sphere r_{ph} and the impact parameter u_{ph}/R_s decrease with charge parameters Q . Furthermore, the impact parameter u_{ph}/R_s for the charged BH with URC DM halo is slightly greater than that for the standard RN ($Q = 0.3$) and smaller than that for standard Schwarzschild BHs see Fig. 9(b) and Table.IV & V. The deflection limit coefficients \bar{a} and \bar{b} for the CDM model as functions of the charge parameter Q are respectively displayed in

Strong Lensing Coefficients			
Q	\bar{a}	\bar{b}	u_{ph}/R_s
Standard Schwarzschild BH	1.00	-0.40023	2.59808
Standard RN BH(0.3)	1.05183	-0.396509	2.42935
0	1.00003	-0.400156	2.59829
0.1	1.00458	-0.399274	2.58083
0.2	1.01976	-0.39711	2.5267
0.3	1.05185	-0.396434	2.429555
0.4	1.12319	-0.413559	2.2732
0.5	1.41414	-0.732937	2.00022

TABLE I: Estimation of strong lensing coefficients \bar{a} , \bar{b} , and u_{ph}/R_s for various values of the charge parameter Q in the context of a charged BH with a URC DM halo, specifically for the M87* BH. The constants used in the calculations are $A = 805.231$ and $B = 3.40611 * 10^{-9}$.

Strong Lensing Coefficients			
Q	\bar{a}	\bar{b}	u_{ph}/R_s
Standard Schwarzschild BH	1.00	-0.40023	2.59808
Standard RN BH(0.3)	1.05183	-0.396509	2.42935
0	1.0000	-0.400226	2.59809
0.1	1.00456	-0.399344	2.58063
0.2	1.01974	-0.39718	2.5265
0.3	1.05183	-0.396505	2.42936
0.4	1.12317	-0.413634	2.273
0.5	1.41421	-0.733188	2.00001

TABLE II: Estimation of strong lensing coefficients \bar{a} , \bar{b} , and u_{ph}/R_s for various charge parameters Q in presence of a URC DM Halo around the Supermassive BH SgrA* with parameters $A = 5738.77$ and $B = 2.6346 * 10^{-11}$.

Parameters	M87*				SgrA*			
	$\theta_\infty(\mu as)$	$S(\mu as)$	r_{mag}	$\Delta T_{2,1}(\text{minutes})$	$\theta_\infty(\mu as)$	$S(\mu as)$	r_{mag}	$\Delta T_{2,1}(\text{minutes})$
Standard Schwarzschild BH	19.9633	0.024984	6.82188	17378.8	26.38	0.0330177	6.82188	11.4973
Standard Reissner Nordström BH(0.3)	18.6668	0.0325876	6.48575	16250.2	24.6692	0.0430665	6.48575	10.7507
0	19.9649	0.0249923	6.8217	17377	26.3827	0.0330183	6.82187	11.4973
0.1	19.8307	0.0256108	6.79076	17260.3	26.2054	0.0338356	6.79093	11.4200
0.2	19.4148	0.0277422	6.68968	16898.2	25.6558	0.0366517	6.68984	11.1805
0.3	18.6683	0.0325976	6.48559	16248.4	24.6693	0.0430672	6.48574	10.7506
0.4	17.4669	0.0449611	6.07368	15202.6	23.0816	0.0594043	6.07377	10.6587
0.5	15.3694	0.107632	4.82406	13376.4	20.3095	0.142238	4.8238	8.85059

TABLE III: Estimating various strong lensing observables for a URC DM halo in the presence of supermassive BHs, specifically M87*, SgrA*, with different values of the charge parameter Q .

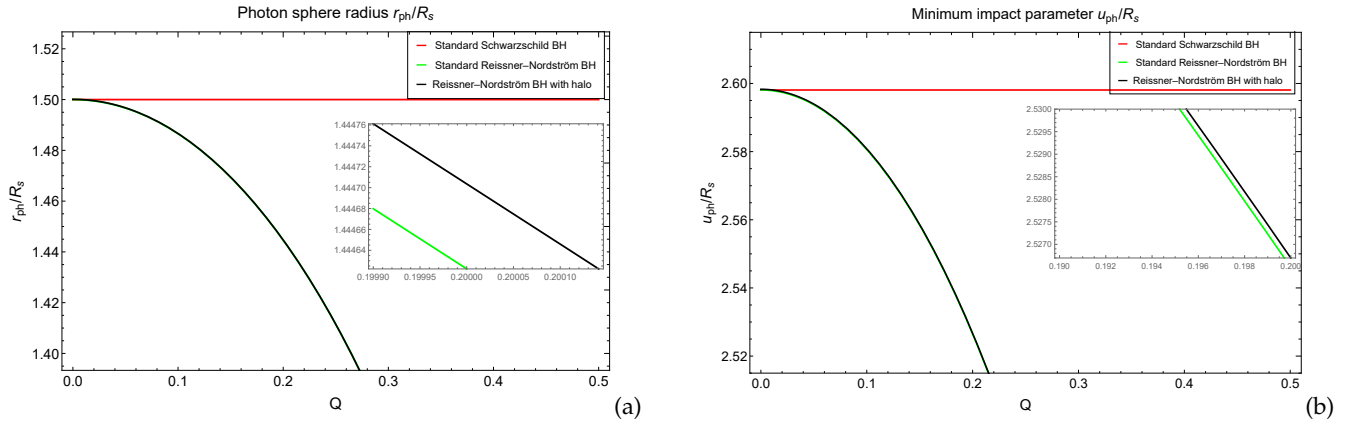


FIG. 1: The left panel depicts the photon sphere radius (r_{ph}/R_s vs Q) and the right panel illustrates the minimum impact parameter (u_{ph}/R_s vs Q) for RN BHs with a URC DM halo (black line), contrasted with standard RN BHs (green line) and standard Schwarzschild BHs (red line). It is noteworthy that both the photon sphere radius (r_{ph}/R_s) and the minimum impact parameter (u_{ph}/R_s) exhibit nearly identical characteristics for the $M87^*$ and $SgrA^*$ scenarios.

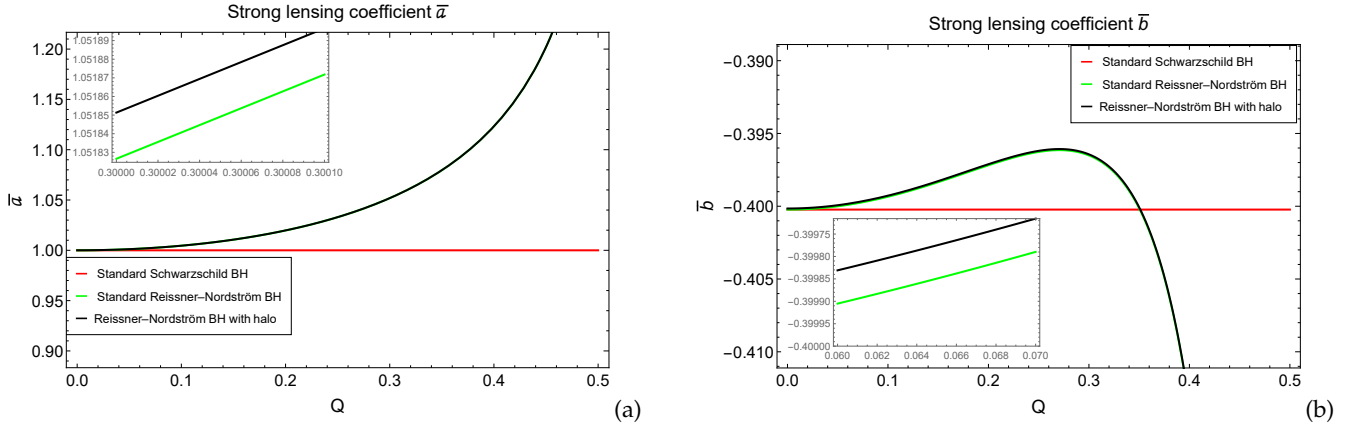


FIG. 2: The left panel illustrates the deflection limit coefficients ($\bar{\alpha}$ vs Q), while the right panel depicts (\bar{b} vs Q) for the RN BH with a URC DM halo (black line), contrasted with standard RN BHs (green line) and standard Schwarzschild BHs (red line). It is noteworthy that the deflection limit coefficients $\bar{\alpha}$ and \bar{b} demonstrate nearly identical characteristics for the $M87^*$ and $SgrA^*$ scenarios.

Fig. 10(a) and Fig. 10(b). It is observed that the deflection limit coefficient $\bar{\alpha}$ increases with Q , while the deflection limit coefficient \bar{b} first increases with Q , then reaches its maximum value and finally decreases with Q . The strong deflection angle, α_D , for the CDM model is depicted in Fig. 11 and as a function of the charge parameter Q . In Fig. 11(b), it is shown as a function of the impact parameter u with different values of the charge parameter Q . In Fig. 11(a), it is observed that the deflection angle α_D increases with the magnitude of the charge parameter Q . The deflection angle for the case of a charged BH with a CDM halo (black solid line) is slightly greater than the case of the standard RN solution (green solid line) as well as the stan-

dard Schwarzschild solution (red solid line). Additionally, the strong deflection angle α_D for the CDM model decreases with the minimum impact parameter u , and it diverges at the critical impact parameter $u = u_{ph}$ at the photon radius $r = r_{ph}$ see Fig. 11(b). From Table VI and Figs. 12, 13, and 14, it is evident that the angular image position θ_∞ and relative magnification r_{mag} decrease with the parameter Q , while the angular separation S increases with the parameter Q . Furthermore, the observable quantity, the angular image position θ_∞ for the case of a charged BH with a CDM halo, is slightly greater than the case of the standard RN solution ($Q = 0.3$) and smaller than the cases of Schwarzschild BHs with a halo, as well as standard Schwarzschild BHs see Fig. 12(a) &

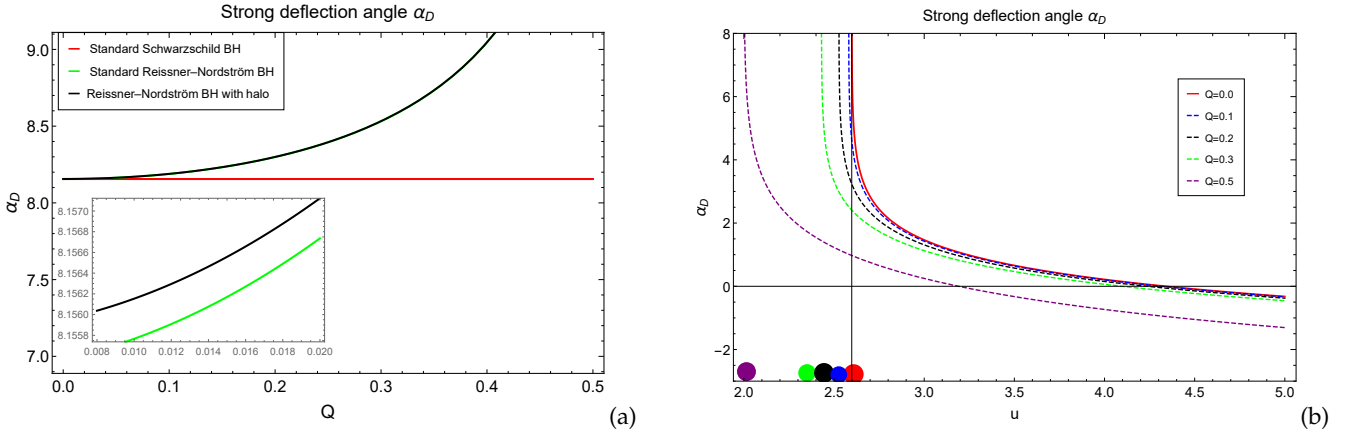


FIG. 3: The left panel depicts the strong deflection angle (α_D) as a function of charge parameter Q at $u = u_{ph} + 0.0002$ for the RN BH with a URC DM halo (black line), contrasting it with the standard RN case (green line) and the standard Schwarzschild BH (red line). In the right panel, the strong deflection angle (α_D) is shown against the impact parameter u for various values of charge parameter Q . The dotted lines indicated in Fig(b) are the value of the impact parameter $u = u_{ph}$, where the deflection angle diverges. It is noteworthy that the strong deflection angle (α_D) exhibits remarkably similar characteristics for both the $M87^*$ and $SgrA^*$ scenarios.

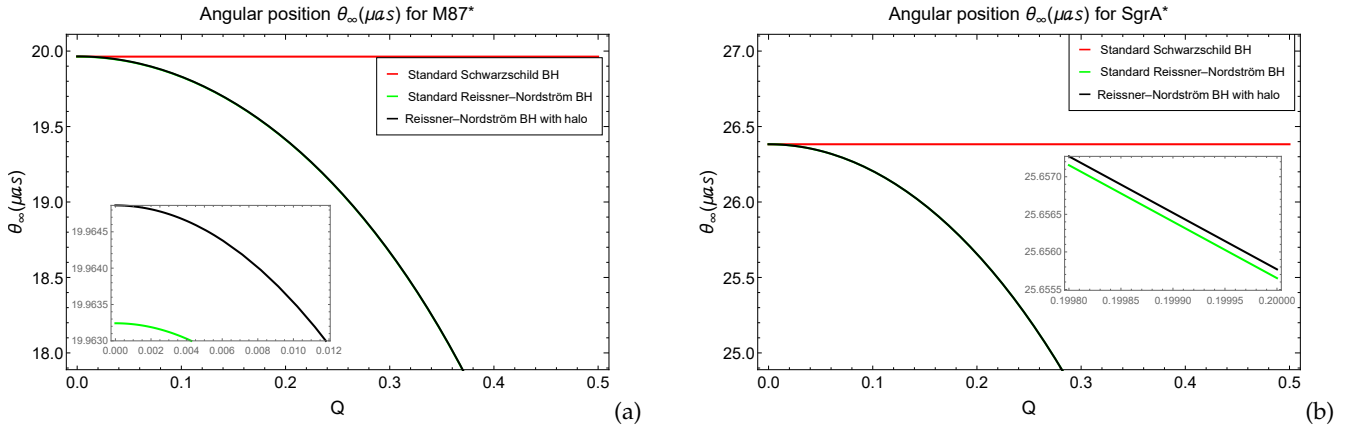


FIG. 4: Comparison of the observable quantity, angular position (θ_∞), versus the parameter Q for both $M87^*$ (left panel) and $SgrA^*$ (right panel). The black line represents the RN solution with a URC DM halo, while the green line corresponds to the standard RN BH and the red line represents the standard Schwarzschild BH.

12(b) and Table VI. On the other hand, the observable quantity, the angular image separation S for the case of a charged BH with a CDM halo, is slightly greater than the cases of the standard RN solution, as well as for the cases of Schwarzschild BHs with a halo and standard Schwarzschild BHs see Fig. 13(a) & 13(b) and Table VI. However, the observable quantity, the relative magnification r_{mag} for the case of a charged BH with a CDM halo, is slightly smaller than the cases of the standard RN solution, as well as for the cases of Schwarzschild BHs with a halo and standard Schwarzschild BHs see Fig. 14 and Table VI. It is crucial to underscore that the photon sphere radius r_{ph}/R_s and the minimum impact parameter u_{ph}/R_s , strong deflection limit coefficients \bar{a}

and \bar{b} , strong deflection angle α_D , and the lensing observable quantity the relative magnification r_{mag} exhibit nearly identical characteristics for the $M87^*$ and $SgrA^*$ scenarios. In Figs. 15(a) & 15(b), the outermost relativistic Einstein rings (θ_n^E) of $M87^*$ and $SgrA^*$ have been depicted for the case of a charged BH with a CDM halo, standard RN, Schwarzschild BH with a halo, and standard Schwarzschild BH. It is observed that the Einstein ring radius is slightly smaller than the cases of standard RN ($Q=0.2$) as well as for the cases of Schwarzschild BH with a halo and standard Schwarzschild BHs. Time delays $\Delta T_{2,1}$ between two different relativistic images with the charge parameter Q are plotted in Figs. 16(a) & 16(b). From these two figures and Table VI, it is found that

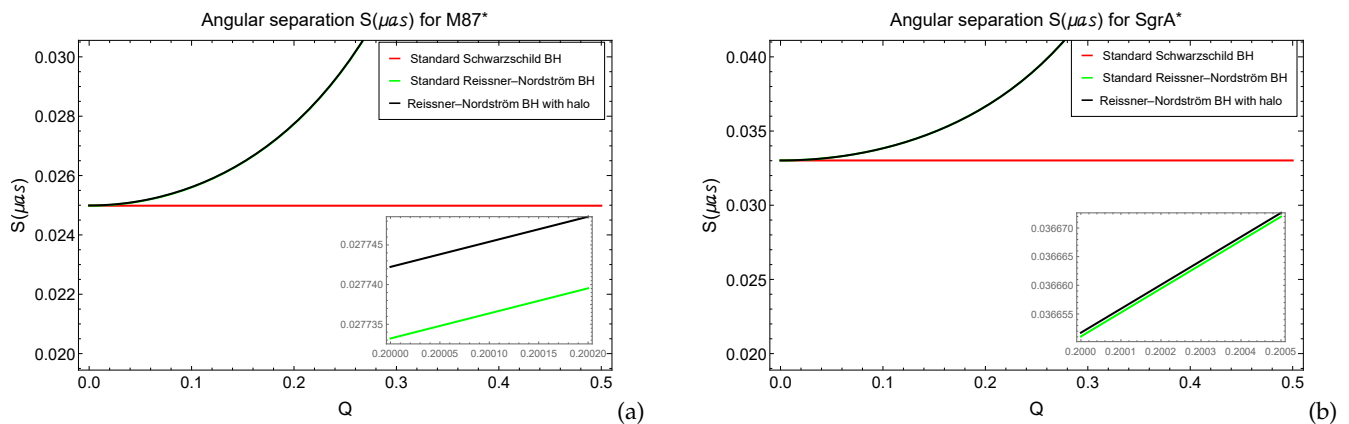


FIG. 5: The figure illustrates the observable angular separation (S) vs Q for $M87^*$ (left panel) and $SgrA^*$ (right panel) within the framework of the RN metric, incorporating a URC DM halo, represented by the black line. This is compared with the predictions of the standard RN BH (green line) and standard Schwarzschild BH (red line).

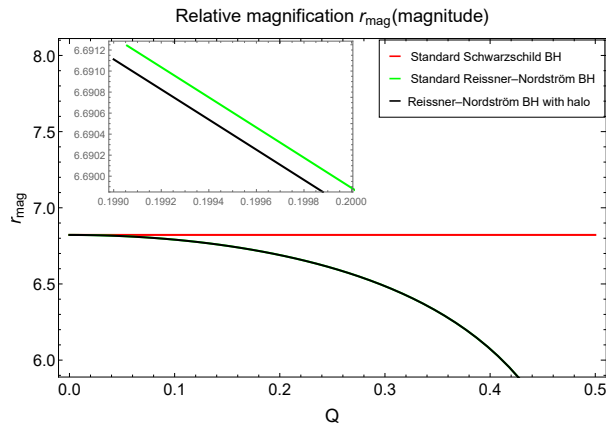


FIG. 6: The observable quantity, relative magnification (r_{mag}) versus Q , is depicted for the RN BH with a URC dark DM halo (black line), in comparison to the standard RN BH (green line) and the standard Schwarzschild BH (red line). It is crucial to emphasize that the relative magnification r_{mag} exhibits nearly identical characteristics for the $M87^*$ and $SgrA^*$ scenarios.

the time delays $\Delta T_{2,1}$ between two different relativistic images decrease with the parameter Q in the context of $M87^*$ and $SgrA^*$ BHs with a CDM halo. It is further observed that the time delays $\Delta T_{2,1}$ are smaller than the cases of standard RN ($Q=0.2$) as well as for the cases of Schwarzschild BH with a halo and standard Schwarzschild BH.

IV. COMPARISON WITH OBSERVATIONS

In this study, we employ the gravitational lensing method developed by Bozza [92] to investigate strong field limit phenomena. This method enables the differentiation of various types of static spherically symmetric BHs and explores their potential astrophysical implica-

tions. We specifically compare observational outcomes for a charged BH with a URC, DM and CDM halo. Additionally, we contrast these results with those of standard RN BHs and Schwarzschild BHs, both with and without halos. To facilitate this comparison, we focus on a supermassive BH, denoted as $SgrA^*$, positioned at the centers of nearby galaxies. We calculate lensing coefficients, namely \bar{a} , \bar{b} , and u_{ph}/R_s , as presented in Tables I, II, IV, V, and VII. Furthermore, we estimate various observable quantities such as θ_∞ , S , and r_{mag} , as outlined in Tables III, VI, and VII. The charged BH scenarios include specific charge values ($Q = 0.2, 0.3$) in conjunction with URC DM and CDM halos. The comparison also encompasses standard RN BHs with a charge of $Q = 0.2$, as well as cases involving Schwarzschild BHs with halos ($Q = 0$) and standard Schwarzschild

Strong Lensing Coefficients			
Q	\bar{a}	\bar{b}	u_{ph}/R_s
Standard Schwarzschild BH	1.00	-0.40023	2.59808
Standard RN BH(0.3)	1.05183	-0.396509	2.42935
0	0.999997	-0.400237	2.59806
0.1	1.00455	-0.399355	2.5806
0.2	1.01973	-0.397191	2.52647
0.3	1.05182	-0.396516	2.42933
0.4	1.12317	-0.413646	2.27297
0.5	1.41422	-0.733228	1.99998

TABLE IV: Estimation for strong lensing coefficients \bar{a} , \bar{b} , and u_{ph}/R_s for various values of the charge parameter Q in the context of a charged BH with a CDM halo around the supermassive BH M87*. The constants are given as $A = 85.508$ and $B = 2.38952 \times 10^{-9}$

Strong Lensing Coefficients			
Q	\bar{a}	\bar{b}	u_{ph}/R_s
Standard Schwarzschild BH	1.00	-0.40023	2.59808
Standard RN BH(0.3)	1.05183	-0.396509	2.42935
0	0.999998	-0.400236	2.59806
0.1	1.00455	-0.399353	2.5806
0.2	1.01973	-0.39719	2.52647
0.3	1.05182	-0.396514	2.42933
0.4	1.12317	-0.413644	2.27298
0.5	1.41422	-0.733223	1.99998

TABLE V: Estimations for the strong lensing coefficients, denoted as \bar{a} and \bar{b} , as well as the ratio u_{ph}/R_s are sought for varying values of the charge parameter Q in the context of a charged BH with a CDM halo, particularly focusing on the supermassive BH SgrA*. The parameters A and B are specified as 6463.81 and 2.537×10^{-11} , respectively.

parameters	M87*				SgrA*			
	$\theta_\infty(\mu as)$	$S(\mu as)$	r_{mag}	$\Delta T_{2,1}(\text{minutes})$	$\theta_\infty(\mu as)$	$S(\mu as)$	r_{mag}	$\Delta T_{2,1}(\text{minutes})$
Standard Schwarzschild BH	19.9633	0.024984	6.82188	17378.8	26.38	0.0330177	6.82188	11.4973
Standard Reissner Nordström BH(0.3)	18.6668	0.0325876	6.48575	16250.2	24.6692	0.0430665	6.48575	10.7507
0	19.96431	0.0249923	6.8219	17378.7	26.3824	0.0330169	6.8219	11.4973
0.1	19.8289	0.0256108	6.79096	17261.9	26.2052	0.0338341	6.79095	11.4200
0.2	19.413	0.0277422	6.68987	16899.8	25.6555	0.0366502	6.68986	11.1805
0.3	18.666	0.0325976	6.48576	16250.1	24.66931	0.0430655	6.48576	10.7506
0.4	17.4652	0.0449611	6.07379	15204.2	23.0813	0.0594023	6.07379	10.6587
0.5	15.3676	0.107632	4.82377	13378.1	20.3092	0.142237	4.82378	8.85059

TABLE VI: Estimate various strong lensing observables for CDM halos in the context of supermassive BHs, specifically M87* and SgrA*, while considering different values of the charge parameter Q .

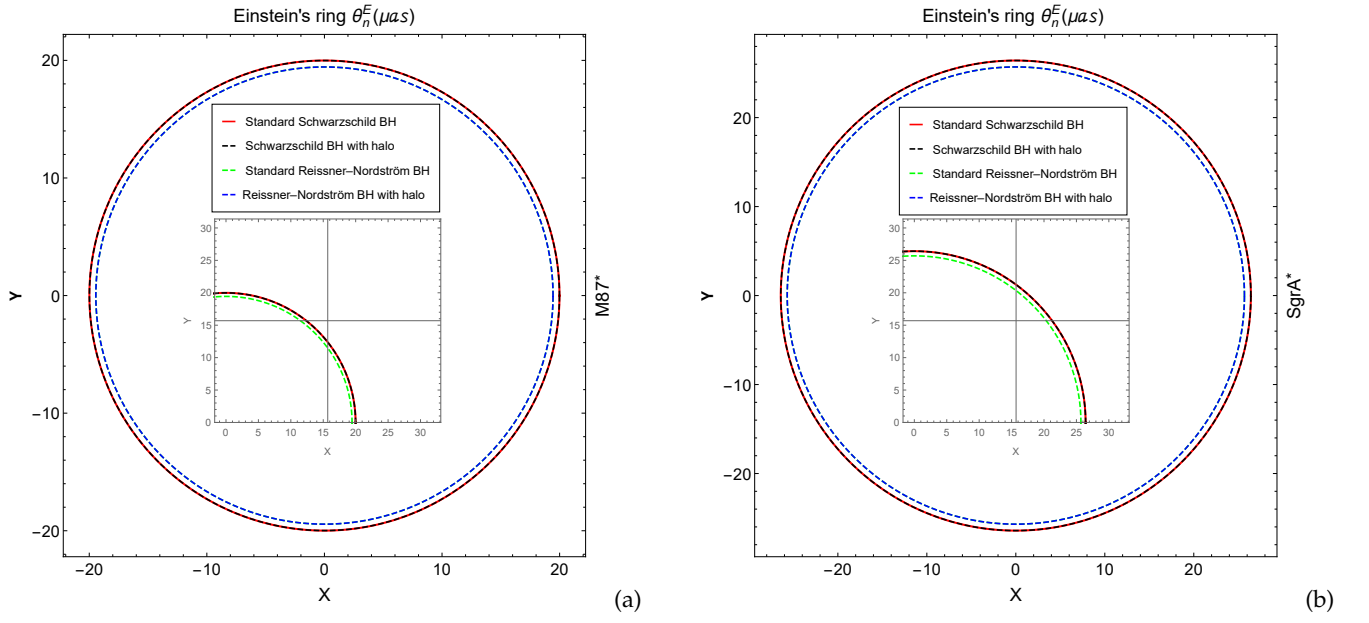


FIG. 7: The observable quantity, Einstein's ring (θ_n^E) plotted against Q , is presented for both $M87^*$ (left panel) and $SgrA^*$ (right panel). The blue dotted line represents the RN BH with a URC DM halo, while the black dotted line corresponds to the Schwarzschild BH with a URC DM halo. Additionally, the green dotted line represents the RN BH without the URC DM halo, and the red solid line corresponds to the standard Schwarzschild BH. This comparison provides insights into the gravitational lensing behavior of these BHs under different configurations.

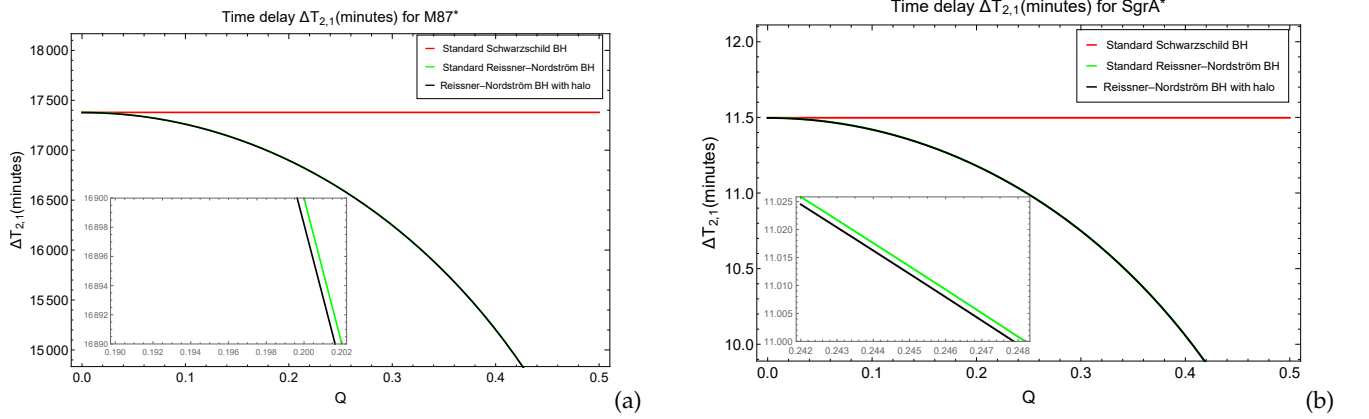


FIG. 8: The observable quantity, time delays ($\Delta T_{2,1}$), is depicted for two relativistic images corresponding to $M87^*$ (left panel) and $SgrA^*$ (right panel). The black line represents the RN solution with a URC DM halo, while the green line corresponds to the standard RN BH, and the red line represents the standard Schwarzschild BH.

BHs ($A = 0, B = 0, \&Q = 0$). Refer to Tables III, VI, and VII for detailed numerical values. In our analysis, we have observed that, considering equal mass and distance for BHs as outlined in Table VII, the angular position of the innermost images, θ_∞ , in the background of a charged BH ($Q = 0.2$) with a URC, DM halo is slightly greater by approximately $0.0001\mu\text{as}$, and with a CDM halo, it is slightly smaller by about $0.0002\mu\text{as}$ compared to the cases of a standard RN BH ($A = B =$

$0, Q = 0.2$). Similarly, the angular separation of images, denoted as S , in the background of a charged BH ($Q = 0.2$) with URC DM halo is slightly greater by approximately $0.0000006\mu\text{as}$, and with CDM halo, it is slightly smaller by about $0.0000009\mu\text{as}$ compared to the cases of a standard RN BH ($A = B = 0, Q = 0.2$). However, the relative magnification, denoted as r_{mag} , in the background of a charged BH ($Q = 0.2$) with URC DM halo is slightly greater by approximately 0.00001 magni-

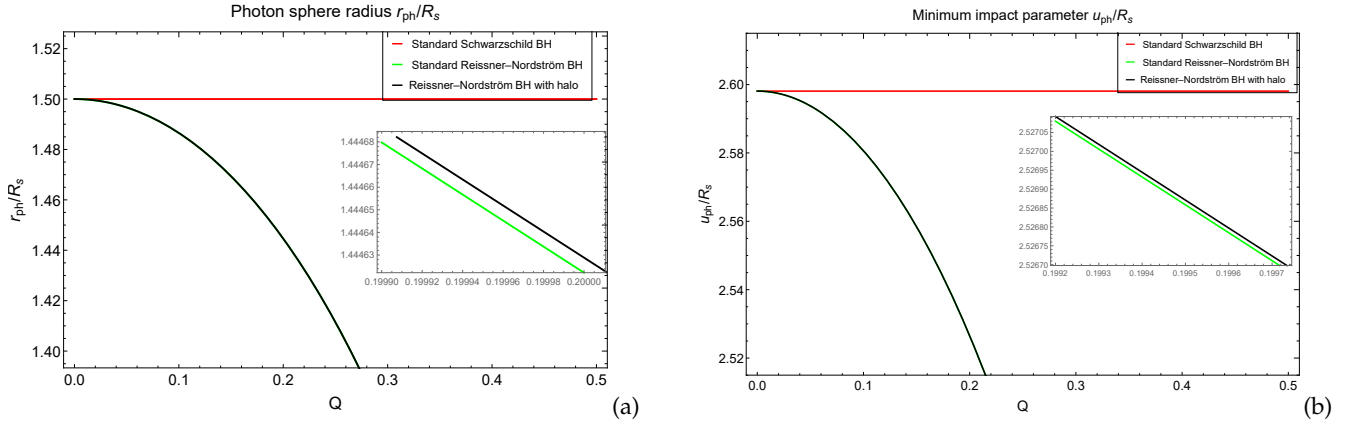


FIG. 9: The left panel depicts the photon sphere radius (r_{ph}/R_s vs Q), while the right panel illustrates the minimum impact parameter (u_{ph}/R_s vs Q) for BHs with a CDM halo (depicted by the black line), in comparison with standard RN BHs (depicted by the green line) and standard Schwarzschild BHs (depicted by the red line). It is crucial to emphasize that both the photon sphere radius (r_{ph}/R_s) and the minimum impact parameter (u_{ph}/R_s) exhibit nearly identical characteristics for the $M87^*$ and $SgrA^*$ scenarios.

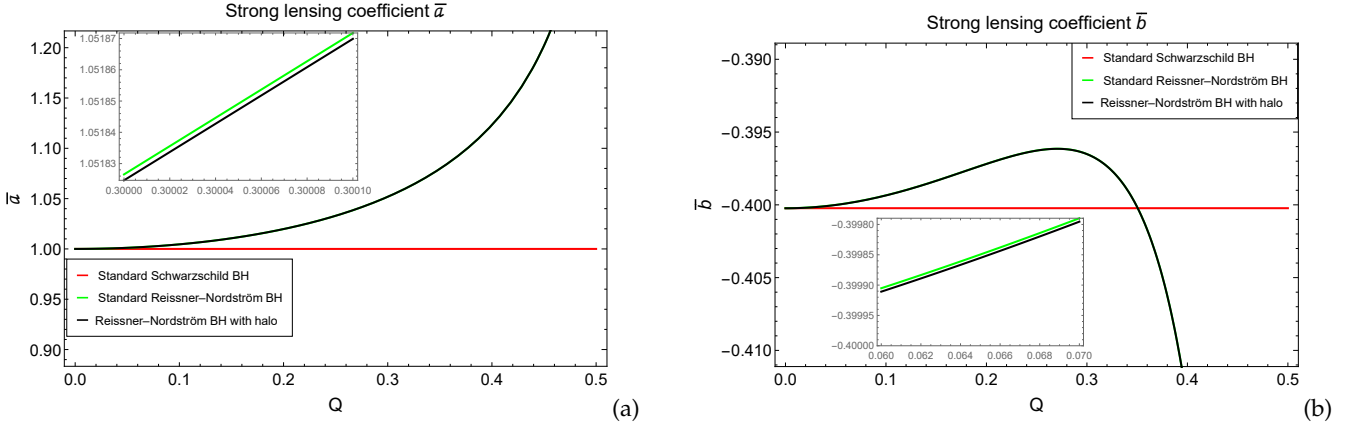


FIG. 10: The left panel displays the deflection limit coefficients (\bar{a} vs Q), while the right panel shows (\bar{b} vs Q) for the RN BH with a CDM halo (depicted by the black line), contrasted with standard RN BHs (green line) and standard Schwarzschild BHs (red line). Notably, it is crucial to underscore that the deflection limit coefficients \bar{a} and \bar{b} exhibit nearly identical characteristics in both the $M87^*$ and $SgrA^*$ scenarios.

tude, and with CDM halo, it is slightly smaller by about 0.00001 magnitude compared to the cases of a standard RN BH ($A = B = 0, Q = 0.2$). It means that the outermost images of the BH with a DM halo are very close to the remaining innermost packed images, making them distinguishable from the other BH images. Furthermore, the observable quantities θ_∞ , S , and r_{mag} in the background of a charged BH ($Q = 0.2$) with URC DM halo are smaller than the cases of a Schwarzschild BH with a halo ($Q = 0$) and a standard Schwarzschild BH ($A = 0, B = 0, Q = 0$). From Figs 7(a) & 7(b) and Figs. 15(a) & 15(b), it is also evident that the Einstein ring radius θ_n^E in the background of a charged BH ($Q = 0.2$) with both the URC DM halo and CDM halo is smaller than

the cases of a standard RN BH ($A = B = 0, Q = 0.2$), a Schwarzschild BH with a halo ($Q = 0$), and a standard Schwarzschild BH ($A = 0, B = 0, Q = 0$). However, one can speculate about how the gravitational field surrounding a charged BH is affected by DM halos. The gravitational field in the vicinity of a BH is enhanced by the existence of DM. The findings from our observations lead to the conclusion that charged BHs, when accompanied by a DM halo (URC & CDM), may be more easily detectable in strong gravitational lensing observations using existing technology. Moreover, if the outermost image can be resolved, it will facilitate the differentiation of a BH with a DM halo from a standard RN BH, a Schwarzschild BH with a halo, and a stan-

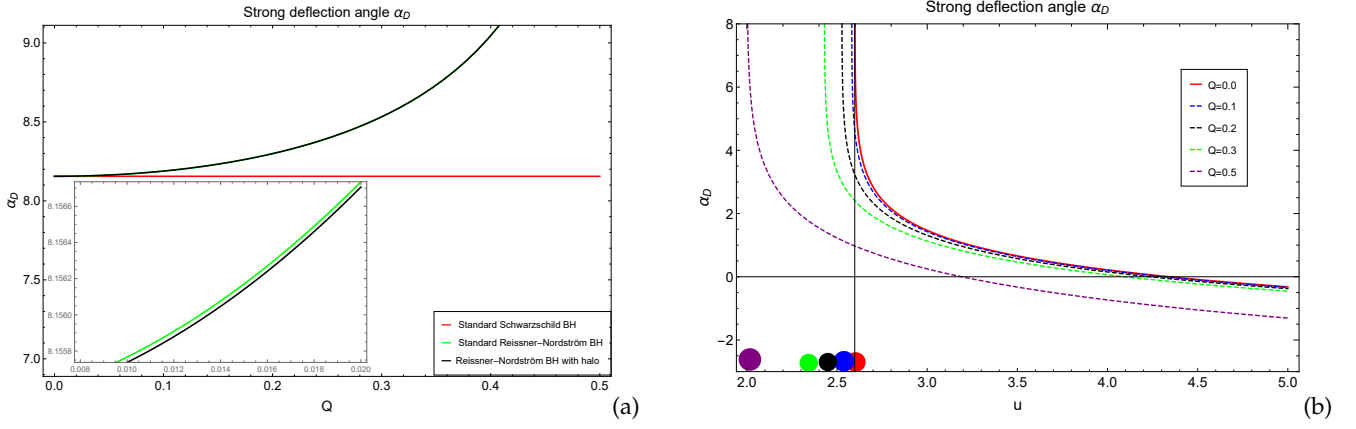


FIG. 11: The left panel illustrates the strong deflection angle (α_D) versus charge parameter (Q) at $u = u_{ph} + 0.0002$ for the RN BH with a CDM halo (depicted by the black line), contrasted with the standard RN case (green line) and the standard Schwarzschild BH (red line). In the right panel, the strong deflection angle (α_D) is plotted with the impact parameter (u) for various values of charge (Q). The dotted lines indicated in Fig(b) are the value of the impact parameter $u = u_{ph}$, where the deflection angle diverges. Notably, the strong deflection angle (α_D) exhibits nearly identical characteristics for both the $M87^*$ and $SgrA^*$ scenarios.

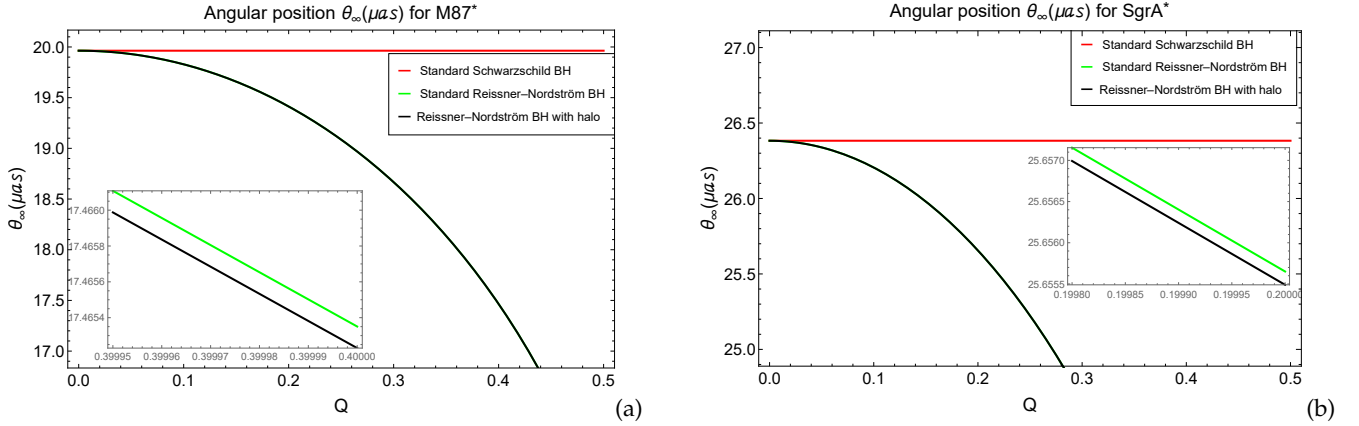


FIG. 12: The observable quantity, angular position (θ_∞) plotted against Q for $M87^*$ (left panel) and $SgrA^*$ (right panel) in the RN BH with a CDM halo (depicted by the black line), as compared to the standard RN solution (green line) and the standard Schwarzschild BH (red line).

standard Schwarzschild BH. It is noteworthy that the gravitational lensing scenario provides a viable method for detecting the audible boundary of sound waves near the charged BH horizon, especially when influenced by DM halos (URC & CDM). The astrophysical implications of these DM halos associated with BHs could offer valuable insights into the connections between the sonic fluid and the shape of BHs. We anticipate that our analytical discoveries will be instrumental in advancing research on BHs and their properties. These findings are expected to support further investigations into the characteristics of the geometry near the event horizon of typical astrophysical BHs.

V. CONSTRAINTS WITH DARK MATTER HALO BY EHT OBSERVATIONS DATA OF $M87^*$ AND $SgrA^*$

In this section, our objective is to ascertain the constraints on the charge parameter of the BH in conjunction with the DM halo, utilizing the observational results from the Event Horizon Telescope (EHT) focused on the $M87^*$ and $SgrA^*$ celestial bodies. The EHT collaboration successfully unveiled the initial images of the BH at the center of the neighboring galaxy, $M87^*$. [114–118, 151]. The discoveries pertaining to the shadow of $M87^*$ offer a captivating exploration into the implications of strong gravitational lensing, providing a robust testing ground for theories of gravity. With a distance of

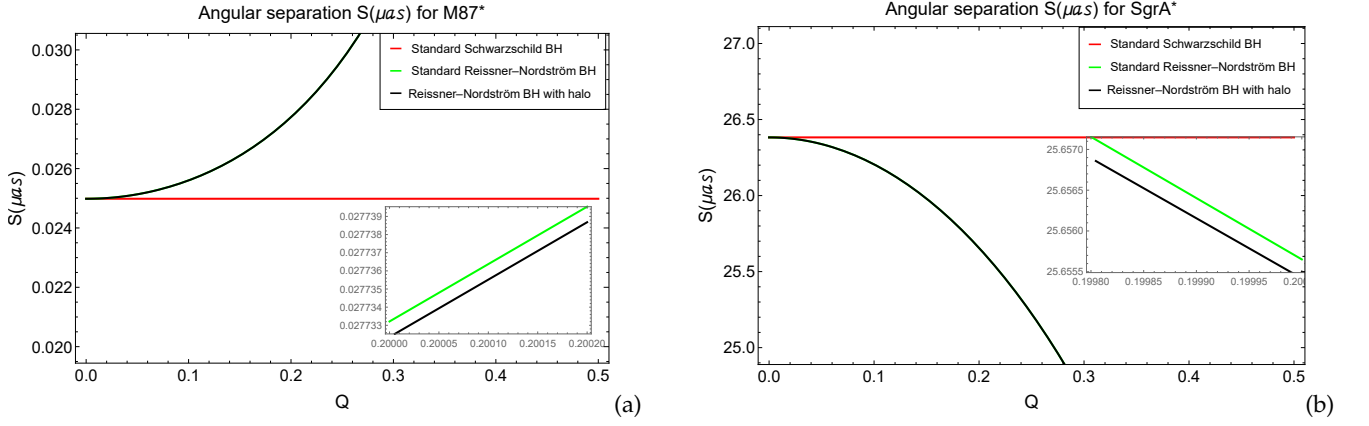


FIG. 13: The observable angular separation (S) vs Q for $M87^*$ (left panel) and $SgrA^*$ (right panel) is depicted. The black line represents the RN solution with a CDM halo, while the green line corresponds to the standard RN BH, and the red line represents the standard Schwarzschild BH.

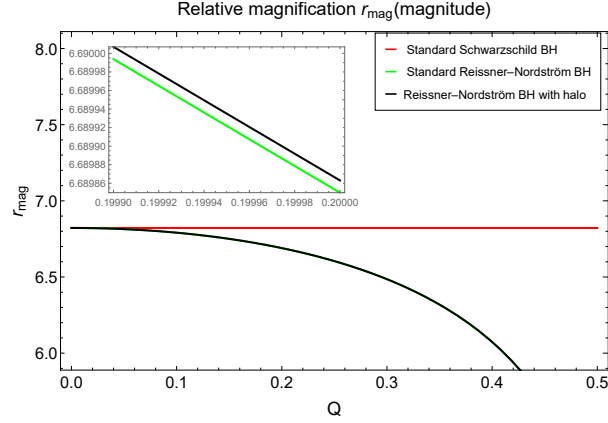


FIG. 14: Comparison of the observable quantity, relative magnification (r_{mag}) versus Q , for the RN BH with a CDM halo (depicted by the black line) in contrast to the standard RN BH (green line) and the standard Schwarzschild BH (red line). Notably, it is crucial to emphasize that the relative magnification r_{mag} demonstrates nearly identical characteristics for both the $M87^*$ and $SgrA^*$ scenarios.

16.8 Mpc, the mass of $M87^*$ is determined to be $(6.5 \pm 0.7) \times 10^9 M_\odot$. The observations by the Event Horizon Telescope (EHT) collaboration reveal an angular diameter of the shadow, denoted as θ_d , to be $42 \pm 3 \mu as$. In a more recent development in 2022, the EHT collaboration unveiled images of the supermassive BH $SgrA^*$ in our Milky Way galaxy. The corresponding angular diameter of its shadow, θ_d , was determined to be $51.8 \pm 2.3 \mu as$, with a mass of $M = (4.3 \pm 0.7) \times 10^6 M_\odot$ and a distance of $d = 8.35$ kpc [152]. Utilizing the observable quantity θ_∞ , which serves as the angular radius of the BH shadow due to strong lensing, we can constrain the charge parameter Q within the 1σ level. Analyzing the EHT results, we find that for $M87^*$ as illustrated in Fig. 17(a), the charge parameter Q for a BH with a URC DM halo is constrained to $0 \leq |Q| \leq 0.366M$. Simi-

larly, for $SgrA^*$ depicted in Fig. 17(b), the constraints are $0 \leq |Q| \leq 0.586M$. In the case of a BH with a CDM halo, the constraints for $M87^*$ shown in Fig. 18(a) are $0 \leq |Q| \leq 0.364M$, while for $SgrA^*$ illustrated in Fig. 18(b), the constraints are $0 \leq |Q| \leq 0.584M$. These findings suggest that charged BHs with a DM halo, whether URC or CDM, conform to the constraints set by the EHT observations. Moreover, the study implies the potential detectability of charged BHs with a DM halo in future observations.

VI. DISCUSSION AND CONCLUSIONS

In this study, we investigated the gravitational lensing effects around charged BHs in the presence of

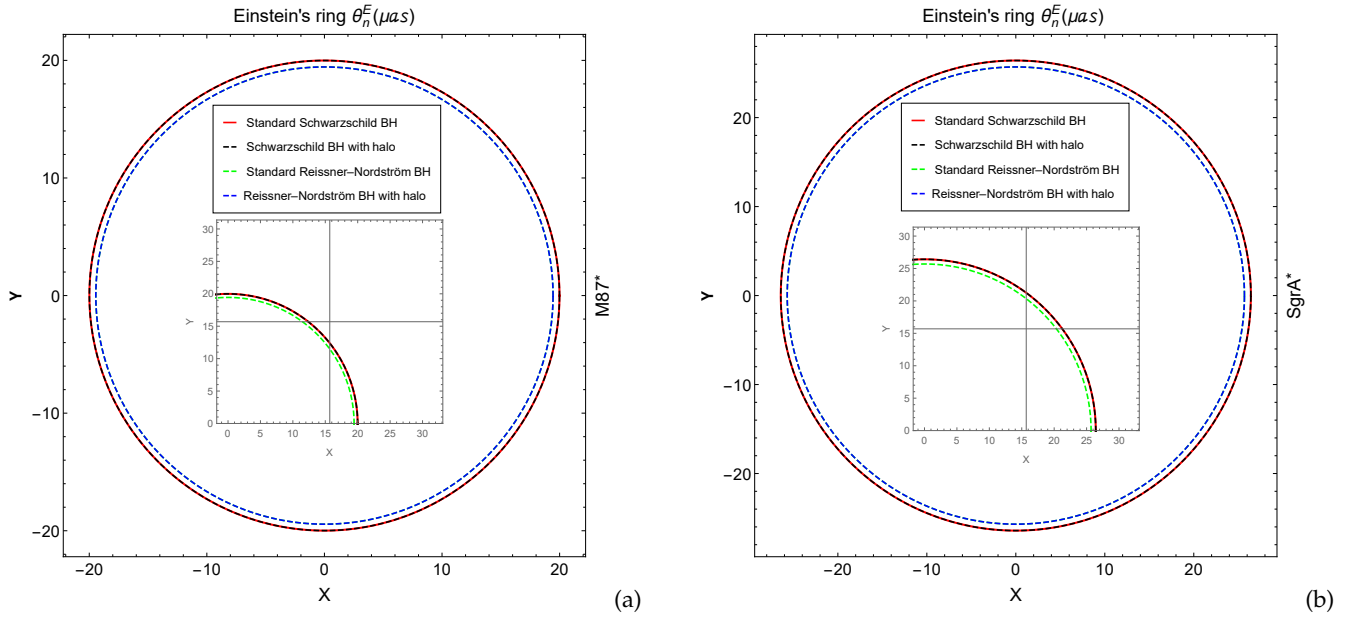


FIG. 15: The observable quantity the Einstein's ring (θ_n^E vs Q) for $M87^*$ (left panel) and for $SgrA^*$ (right panel) for the RN with CDM halo (blue dotted line) in comparison with Schwarzschild with URC DM halo (black dotted line), standard RN (green dotted line) and standard Schwarzschild (red solid line) BHs.

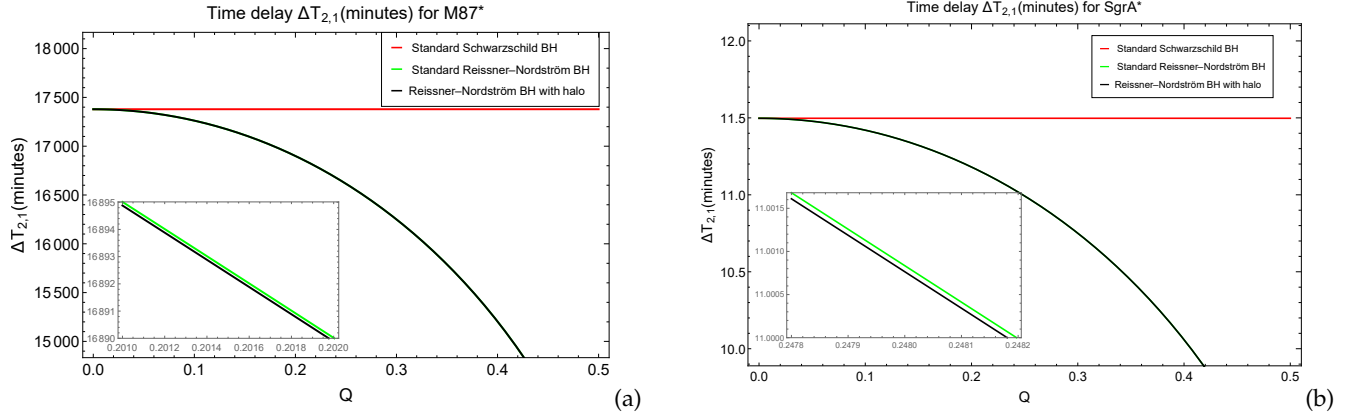


FIG. 16: The observable quantity the time delays $\Delta T_{2,1}$ between two relativistic images for $M87^*$ (left panel) and for $SgrA^*$ (right panel) for the RN with URC DM halo (black line) in comparison with standard RN (green line) and standard Schwarzschild (red line) BHs.

DM halos. Specifically, we focused on supermassive BHs, namely $M87^*$ and $SgrA^*$. Two distinct DM halo models, the URC and CDM models, were considered. The lapse functions corresponding to these models are provided in Eqs (5) and (8). The determination of the parameters involved, such as ρ_0 and r_0 , was achieved through the utilization of observational data pertaining to $M87^*$ and $SgrA^*$.

We have conducted an investigation into the influence of the URC and CDM models, along with the charge parameter Q , on the strong gravitational lensing

phenomenon. Our study encompasses various observable quantities, including the angular position θ_∞ , separation S , relative magnification r_{mag} , Einstein rings for the relativistic images, and time delays $\Delta T_{2,1}$ for relativistic images. We specifically examined these effects in the context of supermassive BHs $M87^*$ and $SgrA^*$. To provide a comprehensive comparison, we contrasted these outcomes with scenarios involving a standard RN BH, a Schwarzschild BH with a halo, and a standard Schwarzschild BH. Firstly, we derive the null geodesic equations for the charged BH spacetime with DM halos using the Hamilton-Jacobi action. Subsequently, we

	Standard Schwarzschild BH	Standard Reissner Nordstrom BH ($Q = 0.2$)	Charged BH for URC model $A = 5738.77$ $B = 2.6346 * 10^{-11}$			Charged BH for CDM model $A = 6463.81$ $B = 2.537 * 10^{-11}$		
			$Q = 0.0$	$Q = 0.2$	$Q = 0.3$	$Q = 0.0$	$Q = 0.2$	$Q = 0.3$
θ_∞ (μas)	26.3826	25.6557	26.3827	25.6558	24.6693	26.3824	25.6555	24.6691
S (μas)	0.0330177	0.0366511	0.0330183	0.0366517	0.043067	0.0330169	0.0366502	0.043066
r_{mag}	6.82188	6.68985	6.82187	6.68984	6.48574	6.8219	6.68986	6.48576
$\Delta T_{2,1}$ (min)	11.4973	11.1805	11.4974	11.1806	10.7507	11.4973	11.1805	10.7506
u_c / R_{sh}	2.59808	2.52649	2.59809	2.5265	2.42936	2.59806	2.52647	2.42933
\bar{a}	1	1.01974	1.0000015	1.01974	1.05183	0.999998	1.01973	1.05182
\bar{b}	-0.40023	-0.397184	-0.400226	-0.39718	-0.396505	-0.400236	-0.39719	-0.396514

TABLE VII: Estimating observables involves considering the supermassive BH (SgrA*), characterized by a mass of $4.3 \times 10^6 M_\odot$ and a distance of 8.35 kpc. This analysis is conducted within the frameworks of the Schwarzschild BH model, the BH URC model, and the BH CDM model.

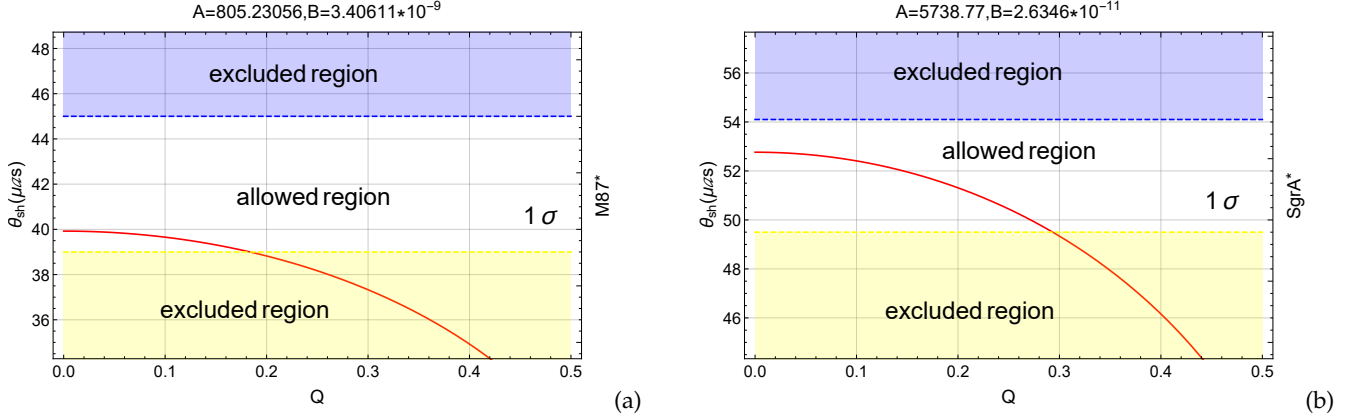


FIG. 17: The angular diameter of shadow $\theta_{sh}(= 2\theta_\infty)$ vs Q for $M87^*$ (left panel) and for $SgrA^*$ (right panel) for the RN with URC DM halo. The allowed (white) region represents the area that is 1σ consistent and the excluded (blue and yellow) region represents the areas that are 1σ inconsistent with EHT observation, suggesting the constraints of the BH charge parameter Q with URC DM halo.

utilize these equations to determine the photon sphere radius, denoted as r_{ph} . It is seen that the radius of photon sphere r_{ph} decreases with the magnitude of the charge parameter Q ; and its value is greater than the corresponding case of standard RN BH and lesser than the corresponding cases of Schwarzschild BH with halo and standard Schwarzschild BH for both the cases of URC DM and CDM halo models.

We numerically and graphically obtained the strong lensing coefficients \bar{a} and \bar{b} , u_{ph}/R_s for both URC and CDM models. It is found that the strong lensing coefficient u_{ph}/R_s are decreased with charge parameters Q and u_{ph}/R_s for the case of charged BH with URC as well as CDM DM halo is a little bit greater than the case of standard RN ($Q = 0.3$) and smaller than the case of

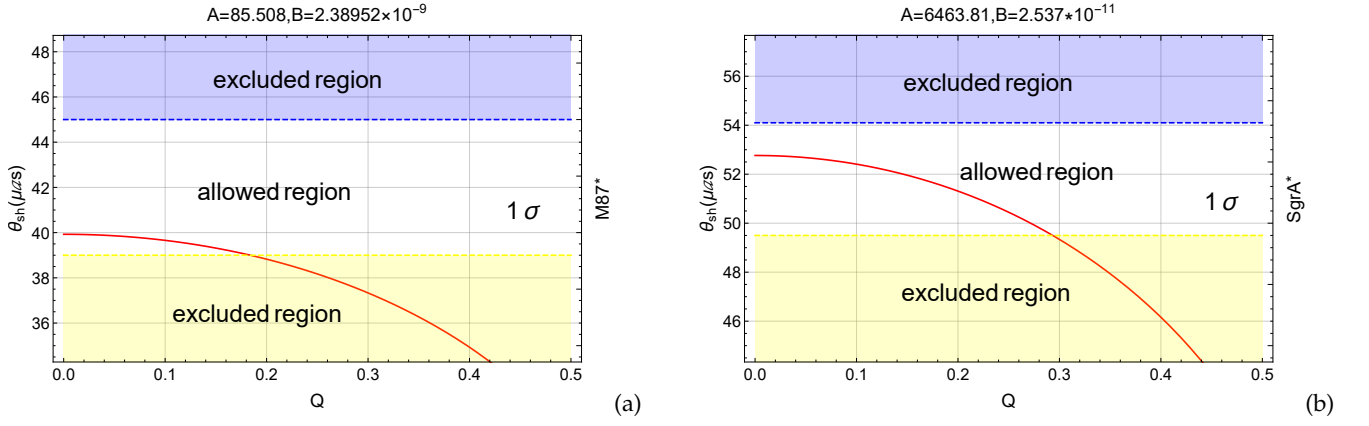


FIG. 18: The angular diameter of shadow $\theta_{sh}(=2\theta_{\infty})$ vs Q for $M87^*$ (left panel) and for $SgrA^*$ (right panel) for the RN with CDM halo. The allowed (white) region represents the area that is 1σ consistent and the excluded (blue and yellow) region represents the areas that are 1σ inconsistent With EHT observation, suggesting the constraints of the BH charge parameter Q with CDM halo.

standard Schwarzschild BHs. The coefficients for strong lensing, denoted as \bar{a} and \bar{b} , in both the scenarios of URC and CDM models vary with the charge parameter Q . Notably, the deflection limit coefficient \bar{a} tends to increase with the magnitude of Q . On the other hand, \bar{b} initially increases with Q , reaches a maximum, and then decreases with further increments in Q . Analyzing the strong deflection angle α_D for both URC and CDM models, it is evident that α_D rises with the magnitude of the charge parameter Q . Moreover, the deflection angle for the case of a charged BH with URC and CDM halo surpasses that of the standard RN (green line) and standard Schwarzschild (red line) BHs. This suggests that the presence of a charged BH parameter with URC and CDM halo enhances gravitational bending effects. Additionally, the strong deflection angle decreases with the minimum impact parameter u and diverges at the critical impact parameter $u = u_{ph}$ corresponding to the photon radius $r = r_{ph}$. This implies that charged BHs, in the presence of a DM halo and sound waves, may exhibit more detectable gravitational bending effects.

The strong lensing observable quantities, the angular image position θ_{∞} , and relative magnification r_{mag} decreases with the parameter Q while angular separation S increases with the parameter Q . Furthermore, the observable quantity, the angular image position θ_{∞} for the cases of URC & CDM halo models is a little bit greater than the case of standard RN ($Q = 0.3$) and smaller than the cases of Schwarzschild BH with halo as well as standard Schwarzschild BHs while the observable quantity, the angular image separation S for the case of charged BH with URC & CDM halo

is a little bit greater than the cases of standard RN as well as for the cases of Schwarzschild BH with halo and standard Schwarzschild BHs, but the observable quantity, the relative magnification r_{mag} for the case of charged BH with URC & CDM halo is a little bit smaller than the cases of standard RN as well as for the cases of Schwarzschild BH with halo and standard Schwarzschild BHs.

In the scenario of the URC DM halo, where $0 \leq Q \leq 0.5$, the angular image position θ_{∞} falls within the range of $15.369 \mu\text{as}$ to $19.965 \mu\text{as}$ for $M87^*$, and $20.3 \mu\text{as}$ to $26.3828 \mu\text{as}$ for $SgrA^*$. Simultaneously, the angular image separation S spans from $0.024 \mu\text{as}$ to $0.1077 \mu\text{as}$ for $M87^*$, and $0.033 \mu\text{as}$ to $0.1423 \mu\text{as}$ for $SgrA^*$. The magnification r_{mag} varies between 4.824 and 6.8218 magnitudes for $M87^*$ and 4.823 to 6.822 magnitudes for $SgrA^*$. In the case of the CDM halo with $0 \leq Q \leq 0.5$, the angular image position θ_{∞} ranges from $15.368 \mu\text{as}$ to $19.9644 \mu\text{as}$ for $M87^*$ and $20.3 \mu\text{as}$ to $26.3825 \mu\text{as}$ for $SgrA^*$. The angular image separation S covers $0.024 \mu\text{as}$ to $0.1077 \mu\text{as}$ for $M87^*$ and $0.033 \mu\text{as}$ to $0.1423 \mu\text{as}$ for $SgrA^*$. The magnification r_{mag} varies within 4.8237 to 6.822 magnitudes for $M87^*$ and 4.8237 to 6.822 magnitudes for $SgrA^*$. It is also observed that the Einstein ring radius θ_n^E in the background of charged BH ($Q = 0.2$) with both the context of URC DM halo and CDM halo is smaller than the cases of standard RN BH ($A = B = 0, Q = 0.2$), Schwarzschild BH with halo ($Q = 0$) and standard Schwarzschild BH ($A = 0, B = 0, Q = 0$). The findings in our observation concluded that the charged BHs, with the presence of DM halo (URC & CDM), might be more easily

detectable in strong gravitational lensing observations using existing technology. Moreover, if the outermost image can be resolved, it will differentiate the BH with a DM halo from standard RN BH, Schwarzschild BH with a halo and standard Schwarzschild BH. This will allow for the characterization of the BHs with a DM halo using existing technology.

Another important astrophysical consequence is the time delay $\Delta T_{2,1}$ between two different relativistic images, which are decreased with the charge parameters Q in the context of $M87^*$ and $SgrA^*$ BHs with URC & CDM halo. It is further observed that the time delay $\Delta T_{2,1}$ is smaller than the cases of standard RN BH ($Q = 0.3$), Schwarzschild BH with URC & CDM halo as well as standard Schwarzschild BH. Deviation of the time delay $\Delta T_{2,1}$ for Charged BH ($Q=0.3$) with URC halo in having the same mass and distance respectively from the standard RN BH ($A = B = 0, Q = 0.3$), Schwarzschild BH with halo ($Q = 0$) and standard Schwarzschild BH ($A = B = Q = 0$) are ~ 2.2 minutes, $\sim 1,129$ minutes and ~ 1130 minutes in the context of $M87^*$ supermassive BH. Deviation of the time delay $\Delta T_{2,1}$ for Charged BH ($Q = 0.3$) with CDM halo in having the same mass and distance respectively from the standard RN BH ($A = B = 0, Q = 0.3$),

Schwarzschild BH with halo ($Q = 0$) and standard Schwarzschild BH ($A = B = Q = 0$) are ~ 0.1 minutes, $\sim 1,128.6$ minutes and ~ 1128.7 minutes in the context of $M87^*$ supermassive BH.

Therefore, the findings in our analysis suggest how the charged BH with DM halo (URC & CDM), is distinguishable from the other astrophysical BHs such as standard RN BH, Schwarzschild BH with URC & CDM halo as well as standard Schwarzschild BH via strong gravitational lensing observation. As a continuation of the present work, we will study strong gravitational lensing using different DM profiles. We also intend to continue working on the charged rotating BHs. Lastly, we may investigate how different BH solutions of modified theories of gravity are affected by DM halos.

VII. ACKNOWLEDGEMENTS

N.U.M would like to thank CSIR, Govt. of India for providing Senior Research Fellowship (No. 08/003(0141))/2020-EMR-I). This research is partly supported by Research Grant F-FA-2021-510 of the Uzbekistan Ministry for Innovative Development. S.C. acknowledges the support of *Istituto Nazionale di Fisica Nucleare* (sez. di Napoli), *Iniziativa Specifiche QGSKY* and *MOONLIGHT2*.

-
- [1] Remo Ruffini and John A Wheeler. Introducing the black hole. *Physics today*, 24(1):30–41, 1971.
 - [2] Valeri Frolov and Igor Novikov. *Black hole physics: Basic concepts and new developments*, volume 96. Springer Science & Business Media, 2012.
 - [3] Stephen W Hawking. Black hole explosions? *Nature*, 248(5443):30–31, 1974.
 - [4] Stephen W Hawking. Black holes and thermodynamics. *Physical Review D*, 13(2):191, 1976.
 - [5] Rosalba Perna, Martyna Chruslinska, Alessandra Corsi, and Krzysztof Belczynski. Binary black hole mergers within the ligo horizon: statistical properties and prospects for detecting electromagnetic counterparts. *Monthly Notices of the Royal Astronomical Society*, 477(3):4228–4240, 2018.
 - [6] Ilias Cholis. On the gravitational wave background from black hole binaries after the first ligo detections. *Journal of Cosmology and Astroparticle Physics*, 2017(06):037, 2017.
 - [7] Barak Zackay, Liang Dai, Tejaswi Venumadhav, Javier Roulet, and Matias Zaldarriaga. Detecting gravitational waves with disparate detector responses: Two new binary black hole mergers. *Physical Review D*, 104(6):063030, 2021.
 - [8] BP Abbott, Richard Abbott, TDea Abbott, S Abraham, F Acernese, K Ackley, C Adams, RX Adhikari, VB Adya, Christoph Affeldt, et al. Gwtc-1: a gravitational-wave transient catalog of compact binary mergers observed by ligo and virgo during the first and second observing runs. *Physical Review X*, 9(3):031040, 2019.
 - [9] Andrzej Królak and Paritosh Verma. Recent observations of gravitational waves by ligo and virgo detectors. *Universe*, 7(5):137, 2021.
 - [10] Chang Liu, Lijing Shao, Junjie Zhao, and Yong Gao. Multiband observation of ligo/virgo binary black hole mergers in the gravitational-wave transient catalog gwtc-1. *Monthly Notices of the Royal Astronomical Society*, 496(1):182–196, 2020.
 - [11] Michal Dominik, Emanuele Berti, Richard O’Shaughnessy, Ilya Mandel, Krzysztof Belczynski, Christopher Fryer, Daniel E Holz, Tomasz Bulik, and Francesco Pannarale. Double compact objects. iii. gravitational-wave detection rates. *The Astrophysical Journal*, 806(2):263, 2015.
 - [12] Horizon Telescope Collaboration. Eht sees black hole shadow. *HIGH-RESOLUTION IMAGING*, page 3, 2019.

- [13] Karl Schwarzschild. On the gravitational field of a point mass according to the einsteinian theory. In *A Source Book in Astronomy and Astrophysics, 1900–1975*, pages 451–455. Harvard University Press, 1979.
- [14] PC Van der Kruit and RJ Allen. The kinematics of spiral and irregular galaxies. *Annual review of astronomy and astrophysics*, 16(1):103–139, 1978.
- [15] Edvige Corbelli and Paolo Salucci. The extended rotation curve and the dark matter halo of m33. *Monthly Notices of the Royal Astronomical Society*, 311(2):441–447, 2000.
- [16] Richard Massey, Thomas Kitching, and Johan Richard. The dark matter of gravitational lensing. *Reports on Progress in Physics*, 73(8):086901, 2010.
- [17] George R Blumenthal, SM Faber, Joel R Primack, and Martin J Rees. Formation of galaxies and large-scale structure with cold dark matter. *Nature*, 311(5986):517–525, 1984.
- [18] Pasquale D Serpico, Vivian Poulin, Derek Inman, and Kazunori Kohri. Cosmic microwave background bounds on primordial black holes including dark matter halo accretion. *Physical Review Research*, 2(2):023204, 2020.
- [19] Daniel B Thomas, Michael Kopp, and Constantinos Skordis. Constraining the properties of dark matter with observations of the cosmic microwave background. *The Astrophysical Journal*, 830(2):155, 2016.
- [20] Varun Sahni, Arman Shafieloo, and Alexei A Starobinsky. Model-independent evidence for dark energy evolution from baryon acoustic oscillations. *The Astrophysical Journal Letters*, 793(2):L40, 2014.
- [21] Bruce Bassett and Renée Hlozek. Baryon acoustic oscillations. *Dark energy: observational and theoretical approaches*, page 246, 2010.
- [22] Tzu-Ching Chang, Ue-Li Pen, Jeffrey B Peterson, and Patrick McDonald. Baryon acoustic oscillation intensity mapping of dark energy. *Physical Review Letters*, 100(9):091303, 2008.
- [23] Samandeep Sharma. Exploring the enigmatic components of the universe. *INTERNATIONAL JOURNAL OF SCIENTIFIC & TECHNICAL DEVELOPMENT*, 2022.
- [24] Graciela B Gelmini. Light weakly interacting massive particles. *Reports on Progress in Physics*, 80(8):082201, 2017.
- [25] Leanne D Duffy and Karl Van Bibber. Axions as dark matter particles. *New Journal of Physics*, 11(10):105008, 2009.
- [26] Alexey Boyarsky, Marco Drewes, Thierry Lasserre, Susanne Mertens, and Oleg Ruchayskiy. Sterile neutrino dark matter. *Progress in Particle and Nuclear Physics*, 104:1–45, 2019.
- [27] Thomas Hambye, Michel HG Tytgat, Jérôme Vandecasteele, and Laurent Vanderheyden. Dark matter from dark photons: a taxonomy of dark matter production. *Physical Review D*, 100(9):095018, 2019.
- [28] Hongwan Liu, Nadav Joseph Outmezguine, Diego Redigolo, and Tomer Volansky. Reviving millicharged dark matter for 21-cm cosmology. *Physical Review D*, 100(12):123011, 2019.
- [29] Paolo Salucci and Annamaria Borriello. The intriguing distribution of dark matter in galaxies. In *Particle Physics in the New Millennium: Proceedings of the 8th Adriatic Meeting*, pages 66–77. Springer, 2003.
- [30] Mark R Lovell, Vincent Eke, Carlos S Frenk, Liang Gao, Adrian Jenkins, Tom Theuns, Jie Wang, Simon DM White, Alexey Boyarsky, and Oleg Ruchayskiy. The haloes of bright satellite galaxies in a warm dark matter universe. *Monthly Notices of the Royal Astronomical Society*, 420(3):2318–2324, 2012.
- [31] Jay Alfred. *Our invisible bodies: Scientific evidence for subtle bodies*. Trafford Publishing, 2007.
- [32] Lorenzo Posti and Amina Helmi. Mass and shape of the milky way’s dark matter halo with globular clusters from gaia and hubble. *Astronomy & Astrophysics*, 621:A56, 2019.
- [33] S. Capozziello, S. Zare, D. F. Mota, and H. Hassanabadi. Dark matter spike around Bumblebee black holes. *JCAP*, 05:027, 3 2023.
- [34] Salvatore Capozziello, Soroush Zare, and Hassan Hassanabadi. Testing bumblebee gravity with global monopoles in a dark matter spike by EHT observations from M87 and Sgr A. 11 2023.
- [35] Shahar Hod. Hairy black holes and null circular geodesics. *Physical Review D*, 84(12):124030, 2011.
- [36] Wolfgang Rindler and Volker Perlick. Rotating coordinates as tools for calculating circular geodesics and gyroscopic precession. *General relativity and gravitation*, 22:1067–1081, 1990.
- [37] Ghulam Mustafa, Farruh Atamurotov, Ibrar Hussain, Sanjar Shaymatov, and Ali Övgün. Shadows and gravitational weak lensing by the Schwarzschild black hole in the string cloud background with quintessential field*. *Chin. Phys. C*, 46(12):125107, 2022.
- [38] Volker Perlick and Oleg Yu Tsupko. Calculating black hole shadows: Review of analytical studies. *Physics Reports*, 947:1–39, 2022.
- [39] Samuel E Gralla, Daniel E Holz, and Robert M Wald. Black hole shadows, photon rings, and lensing rings. *Physical Review D*, 100(2):024018, 2019.
- [40] Matthias Bartelmann. Gravitational lensing. *Classical and Quantum Gravity*, 27(23):233001, 2010.
- [41] Marek A Abramowicz and P Chris Fragile. Foundations of black hole accretion disk theory. *Living Reviews in Relativity*, 16:1–88, 2013.
- [42] G Abbas, H Rehman, Tao Zhu, Qiang Wu, and G Mustafa. Accretion disk around reissner-nordström black hole coupled with a nonlinear electrodynamics field. *arXiv preprint arXiv:2310.04053*, 2023.
- [43] A Ditta, G Mustafa, G Abbas, Farruh Atamurotov, and Kimet Jusufi. Constraining study of circular orbits and accretion disk around nonlinear electrodynamics black hole. *arXiv preprint arXiv:2301.03901*, 2023.
- [44] G Mustafa and Ibrar Hussain. Radial and circular motion of photons and test particles in the schwarzschild

- black hole with quintessence and string clouds. *The European Physical Journal C*, 81(5):419, 2021.
- [45] Faisal Javed, G Mustafa, Saadia Mumtaz, and Farruh Atamurotov. Thermal analysis with emission energy of perturbed black hole in $f(q)$ gravity. *Nuclear Physics B*, 990:116180, 2023.
- [46] Farruh Atamurotov, Ibrar Hussain, G Mustafa, and Kimet Jusufi. Shadow and quasinormal modes of the kerr–newman–kiselev–letelier black hole. *The European Physical Journal C*, 82(9):831, 2022.
- [47] Kostas D Kokkotas and Bernd G Schmidt. Quasi-normal modes of stars and black holes. *Living Reviews in Relativity*, 2:1–72, 1999.
- [48] Edward W Leaver. An analytic representation for the quasi-normal modes of kerr black holes. *Proceedings of the Royal Society of London. A. Mathematical and Physical Sciences*, 402(1823):285–298, 1985.
- [49] Guido D’Amico and Nemanja Kaloper. Black hole echoes. *Physical Review D*, 102(4):044001, 2020.
- [50] Kimet Jusufi, Salvatore Capozziello, Sebastian Bahamonde, and Mubasher Jamil. Testing Born–Infeld $f(T)$ teleparallel gravity through Sgr A* observations. *Eur. Phys. J. C*, 82(11):1018, 2022.
- [51] Andrea Addazi and Salvatore Capozziello. Black hole shadow and chaos bound violation in $f(T)$ teleparallel gravity. *Phys. Lett. B*, 839:137828, 2023.
- [52] Andrea Addazi, Salvatore Capozziello, and Sergei Odintsov. Chaotic solutions and black hole shadow in $f(R)$ gravity. *Phys. Lett. B*, 816:136257, 2021.
- [53] Jürgen Renn, Tilman Sauer, and John Stachel. The origin of gravitational lensing: A postscript to einstein’s 1936 science paper. *Science*, 275(5297):184–186, 1997.
- [54] Charles L Bennett. Astrophysical observations: lensing and eclipsing einstein’s theories. *Science*, 307(5711):879–884, 2005.
- [55] Ian Hacking. Extragalactic reality: The case of gravitational lensing. *philosophy of science*, 56(4):555–581, 1989.
- [56] Joachim Wambsganss. Gravitational lensing in astronomy. *Living Reviews in Relativity*, 1:1–74, 1998.
- [57] Tommaso Treu. Strong lensing by galaxies. *Annual Review of Astronomy and Astrophysics*, 48:87–125, 2010.
- [58] CR Lawrence, DP Schneider, M Schmidt, CL Bennett, JN Hewitt, BF Burke, EL Turner, and JE Gunn. Discovery of a new gravitational lens system. *Science*, 223(4631):46–49, 1984.
- [59] Bhuvnesh Jain and Ludovic Van Waerbeke. Statistics of dark matter halos from gravitational lensing. *The Astrophysical Journal*, 530(1):L1, 2000.
- [60] Nick Kaiser and Gordon Squires. Mapping the dark matter with weak gravitational lensing. *Astrophysical Journal, Part 1 (ISSN 0004-637X)*, vol. 404, no. 2, p. 441–450., 404:441–450, 1993.
- [61] Inh Jee, Sherry H Suyu, Eiichiro Komatsu, Christopher D Fassnacht, Stefan Hilbert, and Léon VE Koopmans. A measurement of the hubble constant from angular diameter distances to two gravitational lenses. *Science*, 365(6458):1134–1138, 2019.
- [62] S. Capozziello and G. Iovane. Probing the nature of compact dark object at the galactic center by gravitational lensing. *Phys. Lett. A*, 259:185–193, 1999.
- [63] S. Capozziello, Vincenzo F. Cardone, and A. Troisi. Gravitational lensing in fourth order gravity. *Phys. Rev. D*, 73:104019, 2006.
- [64] Gulmina Zaman Babar, Farruh Atamurotov, and Abdullah Zaman Babar. Gravitational lensing in 4-D Einstein–Gauss–Bonnet gravity in the presence of plasma. *Phys. Dark Univ.*, 32:100798, 2021.
- [65] Farruh Atamurotov, Ahmadjon Abdujabbarov, and Wen-Biao Han. Effect of plasma on gravitational lensing by a Schwarzschild black hole immersed in perfect fluid dark matter. *Phys. Rev. D*, 104(8):084015, 2021.
- [66] Farruh Atamurotov, Uma Papnoi, and Kimet Jusufi. Shadow and deflection angle of charged rotating black hole surrounded by perfect fluid dark matter. *Class. Quant. Grav.*, 39(2):025014, 2022.
- [67] Farruh Atamurotov and Sushant G. Ghosh. Gravitational weak lensing by a naked singularity in plasma. *Eur. Phys. J. Plus*, 137(6):662, 2022.
- [68] Farruh Atamurotov, Ibrar Hussain, Ghulam Mustafa, and Ali Övgün. Weak deflection angle and shadow cast by the charged-Kiselev black hole with cloud of strings in plasma*. *Chin. Phys. C*, 47(2):025102, 2023.
- [69] Farruh Atamurotov, Mubasher Jamil, and Kimet Jusufi. Quantum effects on the black hole shadow and deflection angle in the presence of plasma*. *Chin. Phys. C*, 47(3):035106, 2023.
- [70] Allah Ditta, Xia Tiecheng, Saadia Mumtaz, Farruh Atamurotov, G. Mustafa, and Ahmadjon Abdujabbarov. Testing metric-affine gravity using particle dynamics and photon motion. *Phys. Dark Univ.*, 41:101248, 2023.
- [71] Niyaz Uddin Molla, Himanshu Chaudhary, Dhruv Arora, Farruh Atamurotov, Ujjal Debnath, and G. Mustafa. Strong Gravitational Lensing by Sgr A* and M87* Black Holes embedded in Dark Matter Halo exhibiting string cloud and quintessential field. 10 2023.
- [72] Farruh Atamurotov, Kimet Jusufi, Mubasher Jamil, Ahmadjon Abdujabbarov, and Mustapha Azreg-Aïnou. Axion-plasmon or magnetized plasma effect on an observable shadow and gravitational lensing of a Schwarzschild black hole. *Phys. Rev. D*, 104(6):064053, 2021.
- [73] Gulmina Zaman Babar, Farruh Atamurotov, Shafqat Ul Islam, and Sushant G. Ghosh. Particle acceleration around rotating Einstein-Born-Infeld black hole and plasma effect on gravitational lensing. *Phys. Rev. D*, 103(8):084057, 2021.
- [74] Ahmadjon Abdujabbarov, Bobomurat Ahmedov, Naresh Dadhich, and Farruh Atamurotov. Optical properties of a braneworld black hole: Gravitational lensing and retrolensing. *Phys. Rev. D*, 96(8):084017, 2017.
- [75] S. Refsdal. The gravitational lens effect. *Mon. Not. Roy. Astron. Soc.*, 128:295, 1964.

- [76] S. Refsdal. On the possibility of determining Hubble's parameter and the masses of galaxies from the gravitational lens effect. *Mon. Not. Roy. Astron. Soc.*, 128:307, 1964.
- [77] P. Schneider, J. Ehlers, and EE Falco. Gravitational lenses. Springer-Verlag. Berlin Inc., New York, 1992.
- [78] AO Petters, H Levine, and J Wambsganss. Singularity theory and gravitational lensing. Birkhäuser, 2001.
- [79] Charles Galton Darwin. The gravity field of a particle. *Proceedings of the Royal Society of London. Series A. Mathematical and Physical Sciences*, 249(1257):180–194, 1959.
- [80] Clarissa-Marie Claudel, K. S. Virbhadra, and G. F. R. Ellis. The Geometry of photon surfaces. *J. Math. Phys.*, 42:818–838, 2001.
- [81] K. S. Virbhadra. Distortions of images of Schwarzschild lensing. *Phys. Rev. D*, 106(6):064038, 2022.
- [82] K. S. Virbhadra. Relativistic images of Schwarzschild black hole lensing. *Phys. Rev. D*, 79:083004, 2009.
- [83] K. S. Virbhadra. Compactness of supermassive dark objects at galactic centers. *Can. J. Phys.*, 102:512, 2024.
- [84] K. S. Virbhadra and C. R. Keeton. Time delay and magnification centroid due to gravitational lensing by black holes and naked singularities. *Phys. Rev. D*, 77:124014, 2008.
- [85] V. Bozza, S. Capozziello, G. Iovane, and G. Scarpetta. Strong field limit of black hole gravitational lensing. *Gen. Rel. Grav.*, 33:1535–1548, 2001.
- [86] V. Bozza, F. De Luca, G. Scarpetta, and M. Sereno. Analytic Kerr black hole lensing for equatorial observers in the strong deflection limit. *Phys. Rev. D*, 72:083003, 2005.
- [87] Simonetta Frittelli, Thomas P. Kling, and Ezra T. Newman. Space-time perspective of Schwarzschild lensing. *Phys. Rev. D*, 61:064021, 2000.
- [88] K. S. Virbhadra, D. Narasimha, and S. M. Chitre. Role of the scalar field in gravitational lensing. *Astron. Astrophys.*, 337:1–8, 1998.
- [89] K. S. Virbhadra and George F. R. Ellis. Schwarzschild black hole lensing. *Phys. Rev. D*, 62:084003, 2000.
- [90] Volker Perlick. On the Exact gravitational lens equation in spherically symmetric and static space-times. *Phys. Rev. D*, 69:064017, 2004.
- [91] Ernesto F. Eiroa, Gustavo E. Romero, and Diego F. Torres. Reissner-Nordstrom black hole lensing. *Phys. Rev. D*, 66:024010, 2002.
- [92] V. Bozza. Gravitational lensing in the strong field limit. *Phys. Rev. D*, 66:103001, 2002.
- [93] Yannick Mellier. Probing the universe with weak lensing. *Ann. Rev. Astron. Astrophys.*, 37:127–189, 1999.
- [94] Matthias Bartelmann and Peter Schneider. Weak gravitational lensing. *Phys. Rept.*, 340:291–472, 2001.
- [95] Catherine Heymans et al. CFHTLenS tomographic weak lensing cosmological parameter constraints: Mitigating the impact of intrinsic galaxy alignments. *Mon. Not. Roy. Astron. Soc.*, 432:2433, 2013.
- [96] Marek Biesiada. Strong lensing systems as a probe of dark energy in the universe. *Phys. Rev. D*, 73:023006, 2006.
- [97] T. M. C. Abbott et al. Dark Energy Survey Year 1 Results: Cosmological constraints from cluster abundances and weak lensing. *Phys. Rev. D*, 102(2):023509, 2020.
- [98] Albert Huber. Remark on the quasiloccal calculation of tidal heating: Energy transfer through the quasiloccal surface. *Phys. Rev. D*, 105(2):024011, 2022.
- [99] Nick Kaiser and Gordon Squires. Mapping the dark matter with weak gravitational lensing. *Astrophys. J.*, 404:441–450, 1993.
- [100] Douglas Clowe, Maruša Bradač, Anthony H Gonzalez, Maxim Markevitch, Scott W Randall, Christine Jones, and Dennis Zaritsky. A direct empirical proof of the existence of dark matter. *The Astrophysical Journal*, 648(2):L109, 2006.
- [101] Farruh Atamurotov, Ahmadjon Abdujabbarov, and Wen-Biao Han. Effect of plasma on gravitational lensing by a Schwarzschild black hole immersed in perfect fluid dark matter. *Phys. Rev. D*, 104(8):084015, 2021.
- [102] Xiaohui Fan et al. The Discovery of a luminous $z = 5.80$ quasar from the Sloan Digital Sky Survey. *Astron. J.*, 120:1167–1174, 2000.
- [103] Chien Y. Peng, Chris D. Impey, Hans-Walter Rix, Christopher S. Kochanek, Charles R. Keeton, Emilio E. Falco, Joseph Lehar, and Brian A. McLeod. Probing the coevolution of supermassive black holes and galaxies using gravitationally lensed quasar hosts. *Astrophys. J.*, 649:616–634, 2006.
- [104] Masamune Oguri and Philip J. Marshall. Gravitationally lensed quasars and supernovae in future wide-field optical imaging surveys. *Mon. Not. Roy. Astron. Soc.*, 405:2579–2593, 2010.
- [105] Minghao Yue, Xiaohui Fan, Jinyi Yang, and Feige Wang. Revisiting the lensed fraction of high-redshift quasars. *The Astrophysical Journal*, 925(2):169, 2022.
- [106] Uros Seljak and Christopher M. Hirata. Gravitational lensing as a contaminant of the gravity wave signal in CMB. *Phys. Rev. D*, 69:043005, 2004.
- [107] Jose M. Diego, Tom Broadhurst, and George Smoot. Evidence for lensing of gravitational waves from LIGO-Virgo data. *Phys. Rev. D*, 104(10):103529, 2021.
- [108] Andreas Finke, Stefano Foffa, Francesco Iacovelli, Michele Maggiore, and Michele Mancarella. Probing modified gravitational wave propagation with strongly lensed coalescing binaries. *Physical Review D*, 104(8):084057, 2021.
- [109] Kai Liao, Zhengxiang Li, Shuo Cao, Marek Biesiada, Xiaogang Zheng, and Zong-Hong Zhu. The Distance Duality Relation From Strong Gravitational Lensing. *Astrophys. J.*, 822(2):74, 2016.
- [110] J. R. Nascimento, A. Yu. Petrov, P. J. Porfirio, and A. R. Soares. Gravitational lensing in black-bounce space-times. *Phys. Rev. D*, 102(4):044021, 2020.
- [111] Haroldo C. D. Lima Junior, Jian-Zhi Yang, Luís C. B. Crispino, Pedro V. P. Cunha, and Carlos A. R. Herdeiro. Einstein-Maxwell-dilaton neutral black holes in strong magnetic fields: Topological charge, shadows, and lensing. *Phys. Rev. D*, 105(6):064070, 2022.

- [112] Niyaz Uddin Molla and Ujjal Debnath. Gravitational lensing for power-Maxwell charged quintessence black hole in Rastall gravity. *Int. J. Geom. Meth. Mod. Phys.*, 19(12):2250183, 2022.
- [113] Niyaz Uddin Molla and Ujjal Debnath. Shadows and strong gravitational lensing by Van der Waals black hole in homogeneous plasma. *Annals Phys.*, 453:169304, 2023.
- [114] Kazunori Akiyama et al. First M87 Event Horizon Telescope Results. II. Array and Instrumentation. *Astrophys. J. Lett.*, 875(1):L2, 2019.
- [115] Kazunori Akiyama et al. First M87 Event Horizon Telescope Results. III. Data Processing and Calibration. *Astrophys. J. Lett.*, 875(1):L3, 2019.
- [116] Kazunori Akiyama et al. First M87 Event Horizon Telescope Results. IV. Imaging the Central Supermassive Black Hole. *Astrophys. J. Lett.*, 875(1):L4, 2019.
- [117] Kazunori Akiyama et al. First M87 Event Horizon Telescope Results. V. Physical Origin of the Asymmetric Ring. *Astrophys. J. Lett.*, 875(1):L5, 2019.
- [118] Kazunori Akiyama et al. First M87 Event Horizon Telescope Results. VI. The Shadow and Mass of the Central Black Hole. *Astrophys. J. Lett.*, 875(1):L6, 2019.
- [119] Sharmanthie Fernando and Sean Roberts. Gravitational lensing by charged black holes. *General Relativity and Gravitation*, 34:1221–1230, 2002.
- [120] V. Bozza and L. Mancini. Time delay in black hole gravitational lensing as a distance estimator. *Gen. Rel. Grav.*, 36:435–450, 2004.
- [121] AS Majumdar and Nupur Mukherjee. Gravitational lensing in the weak field limit by a braneworld black hole. *Modern Physics Letters A*, 20(32):2487–2496, 2005.
- [122] Ernesto F. Eiroa and Gustavo E. Romero. Gravitational lensing of transient neutrino sources by black holes. *Phys. Lett. B*, 663:377–381, 2008.
- [123] Valerio Bozza. Gravitational lensing by black holes: The case of sgr a. 1577(1):89–93, 2014.
- [124] Satyabrata Sahu, Kinjal Lochan, and D. Narasimha. Gravitational lensing by self-dual black holes in loop quantum gravity. *Phys. Rev. D*, 91:063001, 2015.
- [125] Shafqat Ul Islam and Sushant G. Ghosh. Strong field gravitational lensing by hairy Kerr black holes. *Phys. Rev. D*, 103(12):124052, 2021.
- [126] Jefferson de M Toledo and VB Bezerra. Black holes with cloud of strings and quintessence in loveclock gravity. *The European Physical Journal C*, 78:1–12, 2018.
- [127] Salvatore Capozziello and Gamal G. L. Nashed. Charged spherically symmetric black holes in scalar-tensor Gauss-Bonnet gravity. *Class. Quant. Grav.*, 40(20):205023, 2023.
- [128] Gamal G. L. Nashed and Salvatore Capozziello. Charged spherically symmetric black holes in $f(R)$ gravity and their stability analysis. *Phys. Rev. D*, 99(10):104018, 2019.
- [129] G. G. L. Nashed and S. Capozziello. Charged Anti-de Sitter BTZ black holes in Maxwell- $f(T)$ gravity. *Int. J. Mod. Phys. A*, 33(13):1850076, 2018.
- [130] A. M. Awad, S. Capozziello, and G. G. L. Nashed. D -dimensional charged Anti-de-Sitter black holes in $f(T)$ gravity. *JHEP*, 07:136, 2017.
- [131] Paolo Salucci and Andreas Burkert. Dark matter scaling relations. *The Astrophysical Journal*, 537(1):L9, 2000.
- [132] Fiorenza Donato, Gianfranco Gentile, Paolo Salucci, Christiane Frigerio Martins, MI Wilkinson, Gerard Gilmore, EK Grebel, Andreas Koch, and Rosemary Wyse. A constant dark matter halo surface density in galaxies. *Monthly Notices of the Royal Astronomical Society*, 397(3):1169–1176, 2009.
- [133] Paolo Salucci. The distribution of dark matter in galaxies. *The Astronomy and Astrophysics Review*, 27:1–60, 2019.
- [134] Hai-Nan Lin and Xin Li. The dark matter profiles in the milky way. *Monthly Notices of the Royal Astronomical Society*, 487(4):5679–5684, 2019.
- [135] Kimet Jusufi, Mubasher Jamil, Paolo Salucci, Tao Zhu, and Sumarna Haroon. Black hole surrounded by a dark matter halo in the m87 galactic center and its identification with shadow images. *Physical Review D*, 100(4):044012, 2019.
- [136] Julio F Navarro, Carlos S Frenk, and Simon DM White. A universal density profile from hierarchical clustering. *The Astrophysical Journal*, 490(2):493, 1997.
- [137] LJ Oldham and MW Auger. Galaxy structure from multiple tracers—ii. m87 from parsec to megaparsec scales. *Monthly Notices of the Royal Astronomical Society*, 457(1):421–439, 2016.
- [138] Zhaoyi Xu, Xian Hou, Xiaobo Gong, and Jiancheng Wang. Black hole space-time in dark matter halo. *Journal of Cosmology and Astroparticle Physics*, 2018(09):038, 2018.
- [139] K. S. Virbhadra and G. F. R. Ellis. Gravitational lensing by naked singularities. *Phys. Rev. D*, 65:103004, 2002.
- [140] Stephen L. Adler and K. S. Virbhadra. Cosmological constant corrections to the photon sphere and black hole shadow radii. *Gen. Rel. Grav.*, 54(8):93, 2022.
- [141] Naoki Tsukamoto. Strong deflection limit analysis and gravitational lensing of an Ellis wormhole. *Phys. Rev. D*, 94(12):124001, 2016.
- [142] Naoki Tsukamoto. Deflection angle in the strong deflection limit in a general asymptotically flat, static, spherically symmetric spacetime. *Phys. Rev. D*, 95(6):064035, 2017.
- [143] Savitri V. Iyer and Arlie O. Petters. Light’s bending angle due to black holes: From the photon sphere to infinity. *Gen. Rel. Grav.*, 39:1563–1582, 2007.
- [144] Naoki Tsukamoto. Gravitational lensing by using the 0th order of affine perturbation series of the deflection angle of a ray near a photon sphere. *Eur. Phys. J. C*, 83(4):284, 2023.
- [145] Naoki Tsukamoto. Affine perturbation series of the deflection angle of a ray near the photon sphere of a Reissner-Nordström black hole. *Phys. Rev. D*, 106(8):084025, 2022.
- [146] Jitendra Kumar, Shafqat Ul Islam, and Sushant G. Ghosh. Testing Strong Gravitational Lensing Effects of Supermassive Compact Objects with Regular Space-

- times. *Astrophys. J.*, 938(2):104, 2022.
- [147] Albert Einstein. Lens-Like Action of a Star by the Deviation of Light in the Gravitational Field. *Science*, 84:506–507, 1936.
- [148] Sidney Liebes. Gravitational Lenses. *Phys. Rev.*, 133:B835–B844, 1964.
- [149] Fabian Schmidt. Weak Lensing Probes of Modified Gravity. *Phys. Rev. D*, 78:043002, 2008.
- [150] Jacek Guzik, Bhuvnesh Jain, and Masahiro Takada. Tests of Gravity from Imaging and Spectroscopic Surveys. *Phys. Rev. D*, 81:023503, 2010.
- [151] Kazunori Akiyama et al. First m87 event horizon telescope results. i. the shadow of the supermassive black hole. *Astrophys. J. Lett.*, 875:L1, 2019.
- [152] Kazunori Akiyama et al. First Sagittarius A* Event Horizon Telescope Results. I. The Shadow of the Supermassive Black Hole in the Center of the Milky Way. *Astrophys. J. Lett.*, 930(2):L12, 2022.